A TRIDENT SCHOLAR PROJECT REPORT

NO. 533

Exploring the Viability of an All-Fiber Thermal Characterization System

by

Midshipman 1/C Lian R. Dunlevy, USN

UNITED STATES NAVAL ACADEMY
ANNAPOLIS, MARYLAND

USNA-1531-2

REPORT DOCUMENTATION PAGE

Form Approved
OMB No. 0704-0188

1. REPORT DATE *(DD-MM-YYYY)*	**2. REPORT TYPE**	**3. DATES COVERED** *(From - To)*
5-16-23		

4. TITLE AND SUBTITLE
Exploring the Viability of an All-Fiber Thermal Characterization System

5a. CONTRACT NUMBER

5b. GRANT NUMBER

5c. PROGRAM ELEMENT NUMBER

6. AUTHOR(S)
Lian R. Dunlevy

5d. PROJECT NUMBER

5e. TASK NUMBER

5f. WORK UNIT NUMBER

7. PERFORMING ORGANIZATION NAME(S) AND ADDRESS(ES)

8. PERFORMING ORGANIZATION REPORT NUMBER

9. SPONSORING / MONITORING AGENCY NAME(S) AND ADDRESS(ES)
U.S. Naval Academy
Annapolis, MD 21402

10. SPONSOR/MONITOR'S ACRONYM(S)

11. SPONSOR/MONITOR'S REPORT NUMBER(S)
Trident Scholar Report no. 533 (2023)

12. DISTRIBUTION / AVAILABILITY STATEMENT

This document has been approved for public release; its distribution is UNLIMITED.

13. SUPPLEMENTARY NOTES

14. ABSTRACT

In this project, we progress the feasibility of an All-Fiber Frequency Domain Thermoreflectance (FDTR) system through several avenues. 1.) Simulation of the fiber probe in COMSOL coupled with a sensitivity analysis of the system. These sensitivity studies included the probe in a liquid and with the probe contacting a particle. This led to findings for how several parameters such as conductivity of the transducer, thermal boundary conductance with the transducer, and particle size, could affect sensitivity to the surroundings thermal properties. 2.) The Free Space FDTR system was set up and used to characterize transducer alloys. Several experimental techniques, including profilometry, four point probe measurement, and reflectivity measurements were used in tandem with our FDTR system to characterize the potential transducer alloys relative properties, specifically thermoreflectance. 3.) We have constructed the all fiber system ready for validation and have obtained an entirely internal thermoreflectance signal from 4 permutations of novel coated transducers.

15. SUBJECT TERMS
Frequency Domain Thermoreflectance, FDTR, Sensitivity Analysis, Fiber, Thermal Characterization, Thermoreflectance, Transducer

16. SECURITY CLASSIFICATION OF:			**17. LIMITATION OF ABSTRACT**	**18. NUMBER OF PAGES**	**19a. NAME OF RESPONSIBLE PERSON**
a. REPORT	**b. ABSTRACT**	**c. THIS PAGE**		57	**19b. TELEPHONE NUMBER** *(include area code)*

U.S.N.A. --- Trident Scholar project report; no. 533 (2023)

EXPLORING THE VIABILITY OF AN ALL-FIBER THERMAL CHARACTERIZATION SYSTEM

by

Midshipman 1/C Lian R. Dunlevy
United States Naval Academy
Annapolis, Maryland

Certification of Advisers Approval

Associate Professor Brian F. Donovan
Physics Department

Professor Andrew Smith
Mechanical Engineering Department

Professor Brian Jenkins
Electrical and Computer Engineering Department

Acceptance for the Trident Scholar Committee

Professor Maria J. Schroeder
Associate Director of Midshipman Research

USNA-1531-2

Abstract

Currently, there is no convenient way to measure local, microscopic thermal properties of soft and biological materials with single-digit, micron scale resolution or isolate the materials thermal conductivity from that of the thermal contact resistance between the sample and the measurement device. Due to this lack of ability to thermally characterize soft tissue, models for the melting and freezing of soft tissue cannot optimize performance and prevent damage during cryopreservation. In this project, we lay the foundation for an all-fiber Frequency Domain Thermoreflectance (FDTR) characterization system that operates using the same basic working principles as the recently developed free-space FDTR system, which will allow for system portability. These enhanced qualities will allow for the testing of soft and biological materials in advanced microscopy (e.g., electron microscopes) and in environmental chambers to characterize the thermal properties of biological materials through freezing and thawing cycles during typical cryopreservation processes. Our all-fiber FDTR system will therefore provide the scientific community with a method to characterize the local thermal properties of biological materials with simultaneous monitoring of material morphology.

In this project, we progress the feasibility through several avenues. 1. Simulation of the fiber probe in COMSOL coupled with a sensitivity analysis of the system. These sensitivity studies included the probe in a liquid and with the probe contacting a particle. This led to findings for how several parameters such as conductivity of the transducer, thermal boundary conductance with the transducer, and particle size, could affect sensitivity to the surroundings thermal properties. 2. The Free Space FDTR system was set up and used to characterize transducer alloys. Several experimental techniques, including profilometry, four point probe measurement, and reflectivity measurements were used in tandem with our FDTR system to characterize the

potential transducer alloys relative properties, specifically thermoreflectance. 3. We have constructed the all fiber system ready for validation and have obtained an entirely internal thermoreflectance signal from 4 permutations of novel coated transducers.

Through modeling, characterization of transducer alloys, and early success on all fiber FDTR, the background necessary to develop a system capable of thermally characterizing soft and biological materials is well prepared. The sensitivity results, alloy characterization, and proof of concept provide the information necessary to complete and validate the system and use it to measure previously uncharacterized materials.

Key Words: Frequency Domain Thermoreflectance, FDTR, Sensitivity Analysis, Fiber, Thermal Characterization, Thermoreflectance, Transducer

Acknowledgements

Thank you to Dr. Adam Wilson at ARL for collaborating with us on the project and teaching me cosputtering. Thank you to the Office of Naval Research for funding the project. Thank you, Professor Smith, for the safety, Professor Jenkins for making fiber possible, Professor Donovan for inspiring me to keep going, and Professor Warzoha for starting this project and his continued help. Thank you CAPT Forman for the mentorship and coaching me to lead. Thank you Henry for setting the bar and reminding me of mine. Thank you Mom, Dad, and Keehn for making me the man I am.

Contents

Background

At present, there does not exist a mobile experimental method that scientists can use to characterize the local, microscopic thermal properties of soft and biological materials as they change phase during extreme cooling and heating cycles. Existing thermal characterization techniques fail to provide the spatial resolution necessary to gain physical insight into local thermal properties of biological materials (on the order of 10's of μm) and are challenging to integrate into state-of-the-art temperature chambers. Without a method to track the thermal properties of biological materials as a function of temperature, cryopreservation methods cannot be optimized to reduce damage to soft tissue [1], and other cryogenic treatments (e.g., nano-cryosurgery) will remain inefficient[2]. In this project, we take steps towards the development of a mobile and rugged experimental system for potential use in extracting the microscopic thermal properties of soft and biological materials. This will allow the scientific community to accurately characterize the thermal properties of a wide range of microscopic biological materials, including ovum, plasma, and muscle cells. We expect this system to result in the widespread advancement of cryo-based medical techniques and bio-thermal models.

Several macroscopic techniques are available for the thermal characterization of soft and biological materials. Some widely used characterization techniques, which will be described later in this section, include steady-state heat meter bar systems, the 3-ω technique, and optical pump-probe thermoreflectance (e.g., time-domain thermoreflectance, TDTR, or frequency-domain thermoreflectance, FDTR). Steady state heat meter bars utilize a steady heat source and heat sink and provide one dimensional steady state flow across a material that is sandwiched with high pressure between the two meter bars [3]. It is difficult to use this technique seen in Fig. B.1 (a) to characterize soft/biological materials due to the requirement that high pressures be imposed

across the sample structure. Fig B.1(b) shows the 3-ω method which relies on a measurement of the voltage drops across a metal heater with line widths on the order of 10's of microns [4]. The heater doubles as a resistance thermometer due to well-established relationships between resistance and temperature for highly conductive metals. While the technique is applicable for any dielectric solid with a smooth, flat surface, it is difficult to manipulate biological materials in-situ (i.e., within an environmental chamber) to measure ultra-local thermal properties.

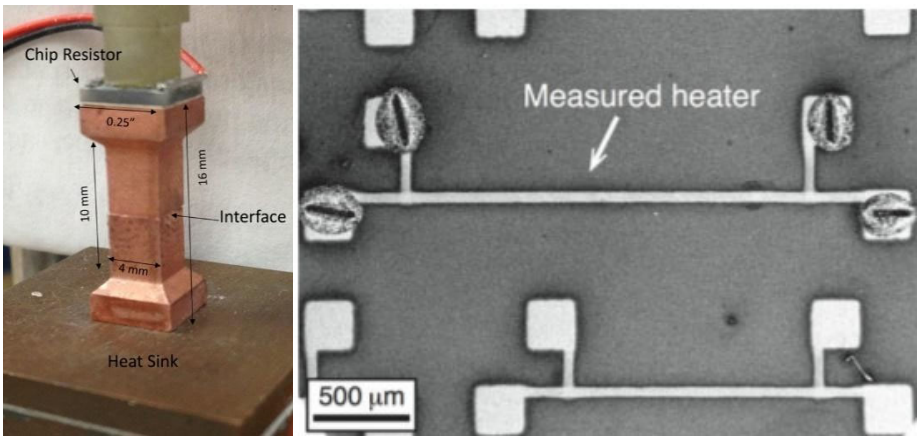

Figure B.1: a) Image of steady state heat meter bars system, and b) image of a patterned heater for use in the 3-omega method

Time-domain thermoreflectance (TDTR) is an optical pump-probe technique that avoids contact with the sample. TDTR probes the changes in temperature on the sample surface as a function of time relative to the arrival of the pump beam (i.e., heat source) [5]. In other words, TDTR measures the change in temperature on a sample surface at different times after a heating event, effectively characterizing the decay of heat as it moves through the sample. The sample's underlying thermal properties can then be determined using an analytical model. The light from the pump laser is converted into heat energy using a transducer, which is often a metal

specifically chosen for its optical properties.. The transducer, a common example being gold, has a known coefficient of thermoreflectance, meaning that it is known how the changes in reflectivity of the surface relate to the temperature, and the probe laser can be used to measure the change in temperature of the surface.

Cahill et al. recently developed a thermoreflectance-based fiber sensor to characterize the thermal properties of soft and biological materials, including egg yolk, pork liver, and butter [6]. In their work, the authors couple a free-space TDTR system to a fiber that can be put in contact with the sample. In this case, both the pump and probe beams are focused into a fiber rather than onto the sample. A metal transducer is deposited onto the end of the fiber tip, rather than on the sample surface, in order to absorb the photonic energy from the pump to thermal energy ahead of the sample. The fiber can then be put into contact with a surrounding liquid or biological material, as shown in Fig. B.2.

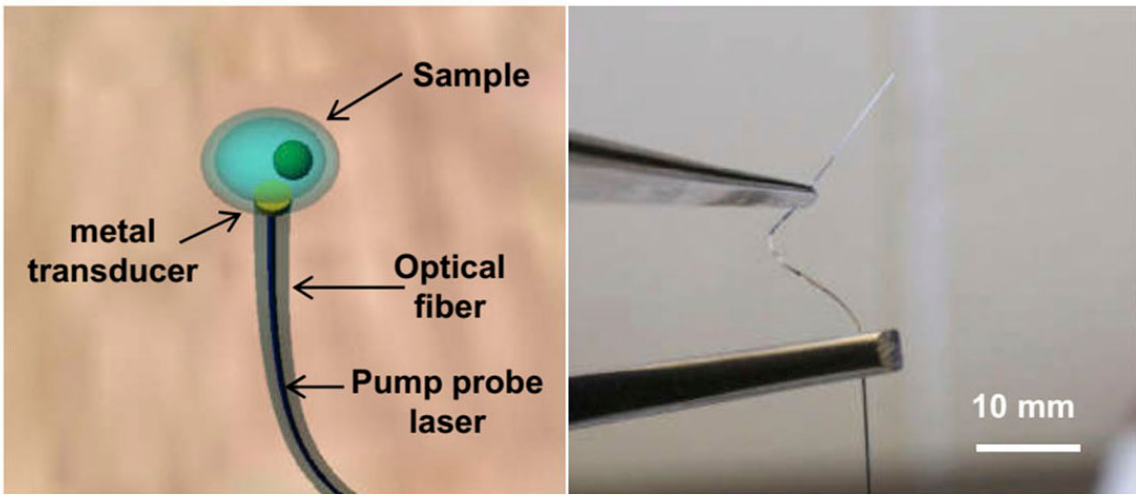

Figure B.2: Aluminum coated fiber tip coupled into free space TDTR system in order to probe the thermal properties of liquid and biological materials. Developed by Prof. David Cahill's group at UIUC [6].

The fiber-based sensor shown in Fig. B.2 serves as a foundational element within our all-fiber system. However, the issue with the use of a free-space TDTR system is its mobility is limited due to the presence of a mechanical delay stage and its extremely large footprint. This deficiency does not allow for the system to be integrated into large microscopy facilities (for example, environmental scanning electron microscopes), which are often required to distinguish between different parts of a biological system. Likewise, the alignment of a free-space system is required to be extremely precise for the system to accurately capture the temperature changes on the sample surface; any slight movement of the optical table itself is likely to result in severe misalignment of the system.

On the other hand, Frequency Domain Thermoreflectance (FDTR) requires no moving parts, and the entire system can be built entirely in fiber, allowing it to travel with a small footprint in order to characterize samples inside of larger imaging facilities (which are required for distinguishing between different regions on the sample). Therefore, we have undertaken development of an all-fiber frequency-domain thermoreflectance system that does not require any moving parts or free-space optics so that these measurements can finally be made in real thermal environments. The system itself will be packaged in a relatively small volume that can be directly integrated into existing microscopy facilities with appropriate fiber ports. Our system is described in detail in a later section. The primary goal of this project is to take steps towards the development of an all-fiber frequency-domain thermoreflectance system.

1. Frequency Domain Thermoreflectance

The foundation for this project is a free space frequency-domain thermoreflectance (FDTR) system capable of measuring the local thermal properties of biological and soft materials using

an all-fiber construction. While previous work by the Cahill group [6] has demonstrated the ability to measure the thermal properties of such materials with a fiber tip coupled to a free-space TDTR system, the use of a free-space optics and time-domain measurements prohibit mobility. If the system is to be integrated with advanced, large-scale microscopes, it must be mobile. Instead, we use FDTR because it has no moving parts and similar measurement capabilities.

It is useful to first discuss the standard components in a free-space FDTR system (i.e., FDTR configured such that the laser beams are “free-space”, or exposed to the environment). This year we moved labs and completely rebuilt, the free-space FDTR system previously in the NEaTT lab. The system schematic is shown in Fig. 1.1, below.

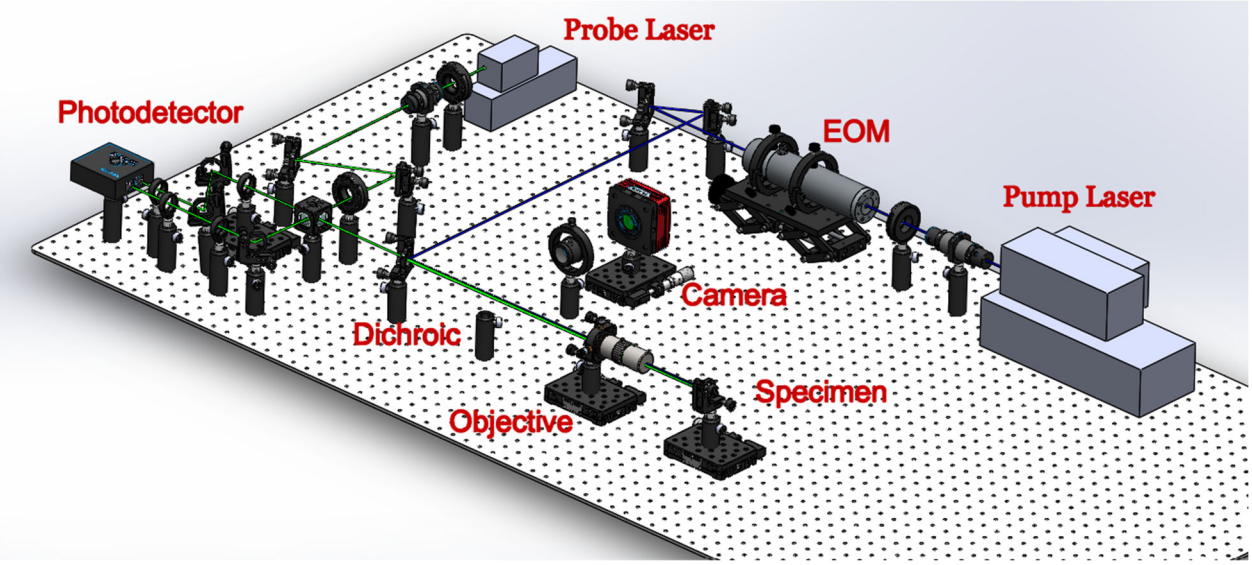

Figure 1.1: Free-space Frequency Domain Thermoreflectance table model

FDTR uses a modulated pump beam to heat the sample surface, which is coated with a metal transducer (typically Au above a thin Ti layer for improved adhesion). The pump beam is modulated using an electro-optic modulator that is connected to a function generator. The transducer serves to convert the photonic energy of the pump to thermal energy on the surface of the sample of interest. Prior to reaching the transducer, the pump beam is steered through an objective lens with a dichroic mirror (i.e., a mirror that preferentially reflects specific

wavelengths of light), after which point it is focused on to the sample. A separate probe beam is directed through the dichroic mirror and is focused down collinearly with the pump beam onto the sample surface. The tube lens and camera on the translation stage are used to ensure the probe beam is centered within the pump beam. This is accomplished by temporarily putting a pellicle, an optic that reflects a small percentage of incoming light, in the post holder, redirecting the beams into the camera for focusing as seen in Fig. 1.2.

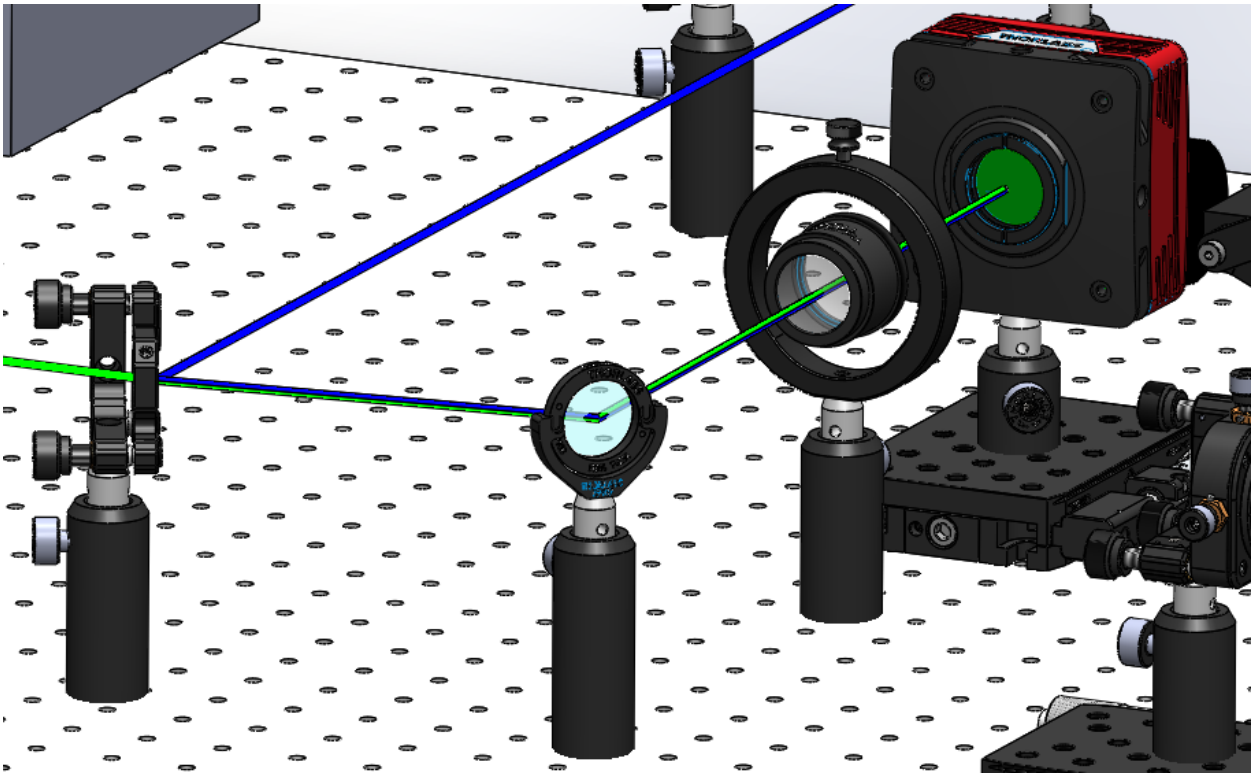

Figure 1.2: Pellicle inserted into post mount to redirect collinear beams into camera for alignment.

With the beams focused and collinear and the pellicle removed, the probe beam is reflected back through the dichroic mirror and focused down onto a photodetector, where its intensity is monitored as a function of the pump's modulation frequency. In this case, the intensity of the probe beam directly corresponds to the magnitude of the reflection at the transducer surface, which itself is a direct function of temperature.

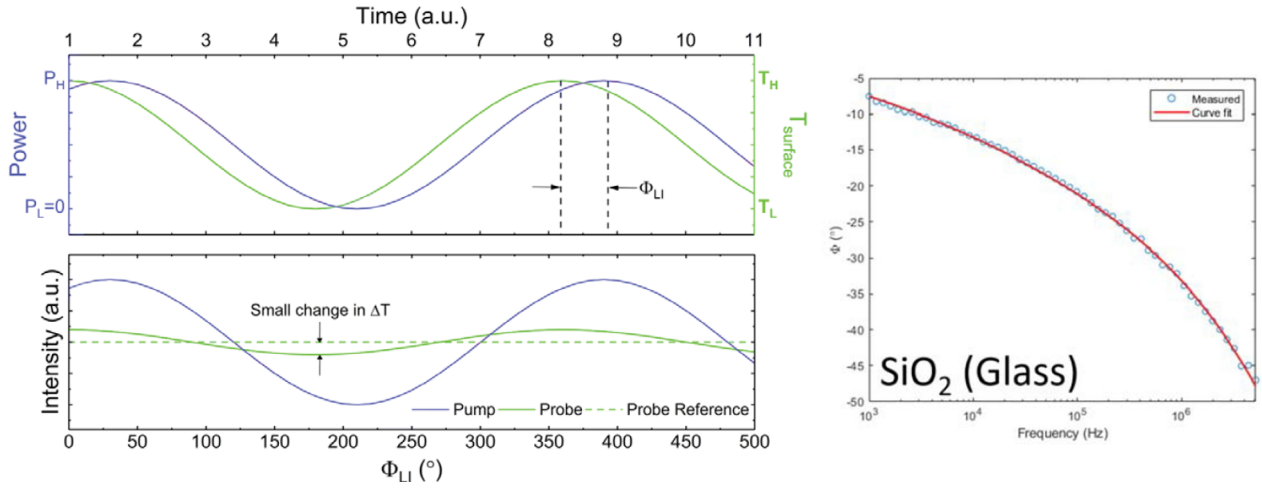

Figure 1.3: (left) The phase lag ϕ_{LI} is determined by analyzing the applied pump power and measured temperature of the surface with the probe beam. (right) Measuring this phase lag over a range of applied pump heating frequencies allows the determination of thermal properties.

Because the temperature at the surface lags behind the imposed heat load (much the same way that the temperature of water in a pot on the stove lags behind the applied heat load below it), we observe a phase lag between the temperature response and the applied heat load in the frequency domain as seen in Fig. 1.3(a). By varying the pump modulation frequency over a wide range, we can vary the thermal penetration depth (i.e., the depth that heat penetrates the sample) to achieve sensitivity to the thermal properties of multiple underlying layers as seen in Fig. 1.3(b). The thermal penetration depth is represented in the schematic below.

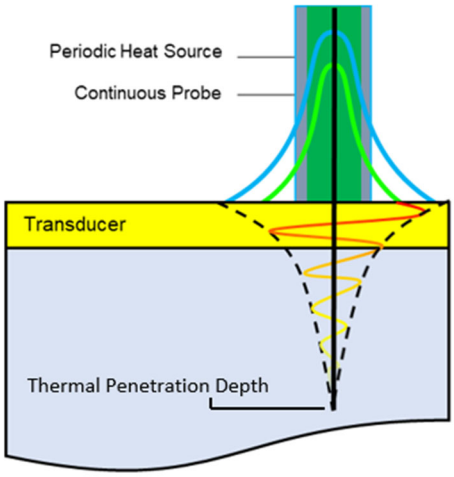

Figure 1.4: Gaussian boundary conditions and thermal penetration depth above the transducer in a multilayer material using free-space FDTR.

The equation that governs heat flow (and the temperature distribution) within the material system shown in Fig. 1.4 is represented by Equation 1.1,

$$\frac{\kappa_r}{r}\frac{\partial}{\partial r}\left(r\frac{\partial \theta}{\partial r}\right)+\kappa_z\frac{\partial^2\theta}{\partial z^2}=C_p\frac{\partial \theta}{\partial t} \tag{1.1}$$

Here θ represents temperature, κ_r the radial thermal conductivity, κ_z the through-plane thermal conductivity, C_p the volumetric heat capacity, and t the time. A Fourier transform is applied to convert the system to the frequency domain. The result is Equation 1.2.

$$\kappa_z\frac{\partial^2\theta(\omega,k,z)}{\partial z^2}=\left(\kappa_r k^2+C_p i\omega\right)\theta(w,k,z) \tag{1.2}$$

Both sides are divided by κ_z, the cross-plane thermal conductivity, and the right side is simplified using q^2.

$$q^2=\frac{\kappa_r k^2+C_p i\omega}{\kappa_z} \tag{1.3}$$

A matrix system is applied to obtain the surface temperatures at both sides of each individual material layer, where b represents the bottom of the n^{th} later, t represents the top of the n^{th} layer, and G is the thermal boundary conductance between material layers (or the amount of heat that can cross a specific interface).

$$\left[\theta_{n,b}\, f_{n,b}\right] = \left[cosh(qd)\ -\frac{1}{\kappa_z q} sinh(qd)\ -\kappa_z q sinh(qd)\, cosh(qd)\right]\left[\theta_{n,t}\, f_{n,t}\right] \quad (1.4)$$

$$\left[\theta_{n+1,t}\, f_{n+1,t}\right] = \left[1\ -G^{-1}\ 0\ 1\right]\left[\theta_{n,b}\, f_{n,b}\right] \quad (1.5)$$

The surface temperature is obtained through matrix multiplication. The M's in Equation 1.6 represent the two matrices in Equation 1.4 and 1.5, for each layer and interface. θ_t is determined via Equation 1.7 and represents the temperature at the top of the transducer (where the measurement occurs). Here, f_t represents the heat flux applied at the sample surface with the pump beam.

$$\left[\theta_b\, f_b\right] = M_n M_{n-1} \cdots M_2 M_1 = [A\ B\ C\ D\ ]\left[\theta_t\, f_t\right] \quad (1.6)$$

$$\theta_t = \frac{D}{C} f_t \quad (1.7)$$

Due to the Gaussian intensity distribution of the probe beam, we use a Hankel transform to obtain the temperature at the top of the transducer surface and within the diameter of the probe beam (Eqn. 1.8). The parameters w_0 and w_1 represent the pump and probe diameters, respectively. A_0 represents the power of the pump beam.

$$H(\omega) = \frac{A_0}{2\pi}\int_0^\infty k\left(-\frac{D}{C}\right) exp\left[-\frac{k^2(w_0^2+w_1^2)}{8}\right] dk \quad (1.8)$$

Finally, we take the inverse tangent of the ratio of the imaginary and real parts of the Hankel transform in order to solve for the phase lag at the sample surface. ϕ_{ext} represents the external phase lag incurred by external system components, like the cables used to connect the

photodetector to the lock-in amplifier. With a thermal model expressed in term of the phase lag as shown in equation 1.9, we can fit the final expression for phase lag to our data dividing the imaginary and real components of the Hankel transformation and extract relevant thermal properties.

$$\phi_{LI} = tan^{-1}\frac{J(H(\omega))}{R(H(\omega))} + \phi_{ext} \tag{1.9}$$

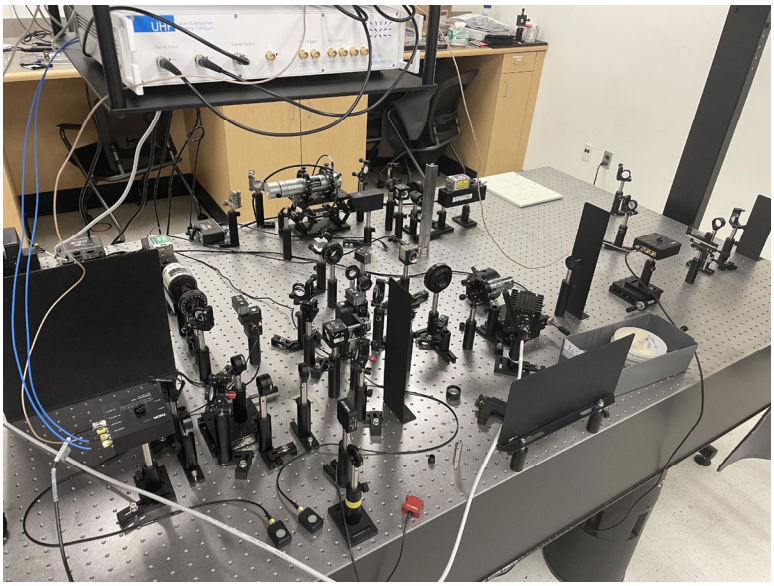

Figure 1.5: The free space FDTR system is now set up in our lab and is seen above

Above in Fig 1.5 the free space FDTR system in our new lab is shown. The system previously setup in a Chauvenet lab, but over the summer the system was moved to our current lab in Rickover. This naturally, with a highly sensitive optical set up, was not a seamless process. We had to work to realign the entire system and in the process found power fluctuations coming from the pump laser. These fluctuations prevented proper alignment and reliable samples from being taken. After some trouble shooting we determined that we would have to swap the laser

out. Our Coherent Genesis MX, capable of power up to 1 W, was swapped out with a Coherent OBIS, capable of power up to 200 mW, both seen in Fig 1.6 below.

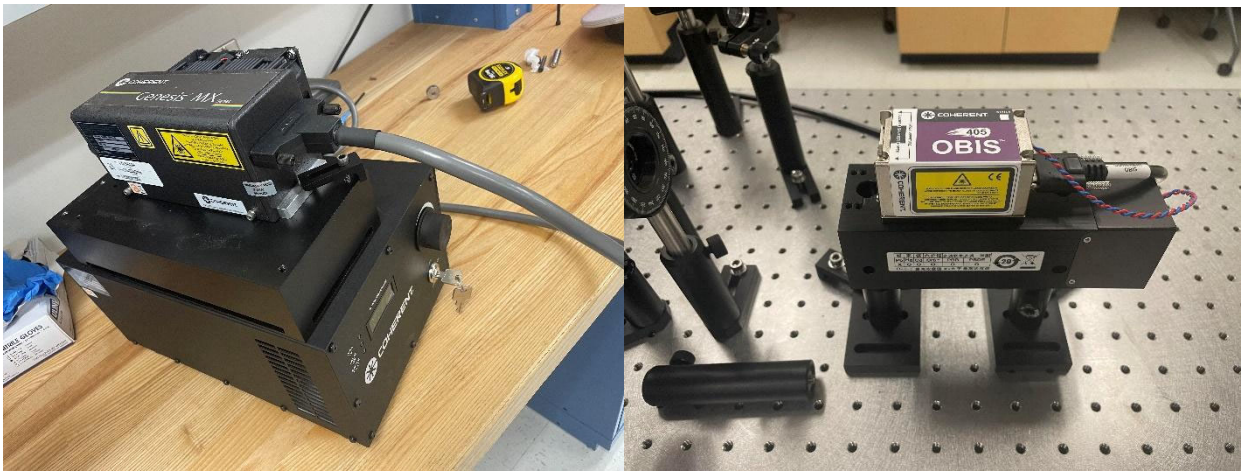

Figure 1.6: On the left is the Coherent Genesis and the right the Coherent OBIS that replaced it. This highlights the size difference and gives a hint at the high power capabilities that we are losing in the swap.

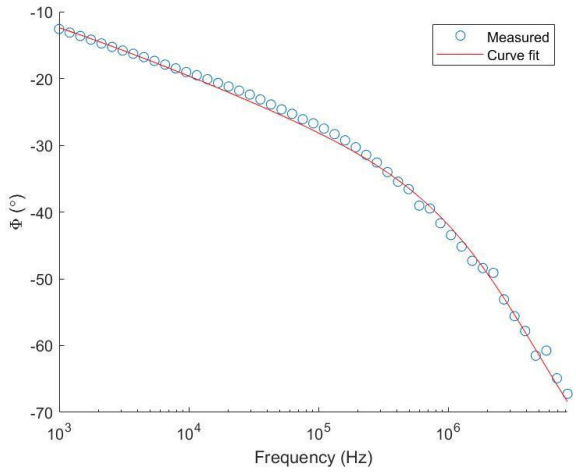

Figure 1.7: Above is a preliminary scan taken with the FTDR system in the Rickover lab. It shows phase lab vs frequency for a sample of gold plated on a glass wafer.

With the Genesis replaced by the OBIS and the system corrected and aligned, we were able to take successful scans. This allowed us to begin testing potential materials for the transducer of

our fiber probe. One of the scans from the new system for a gold transducer sample on glass can be seen in Fig. 1.7 above.

2. Fiber FDTR

The all-fiber system is modeled to match the same theory used in the free-space system. The pump laser couples into an Acousto-Optic Modulator (Brimrose AOM) that accomplishes the same task as the EOM in the free-space system: modulating the pump signal. The wideband multimode recirculators allow flow through the input to the outputs, and between the two output fibers. These recirculators allow the signal from the probe beam to return to the photodetector without permitting the pump beam to "recirculate" in the same direction; this serves the same purpose as the dichroic mirror and polarization optics in the free-space system. The "testing fiber", which contains the transducer that comes into contact with the sample, is coupled to the recirculator path. The entire system is shown in Fig. 2.1, below.

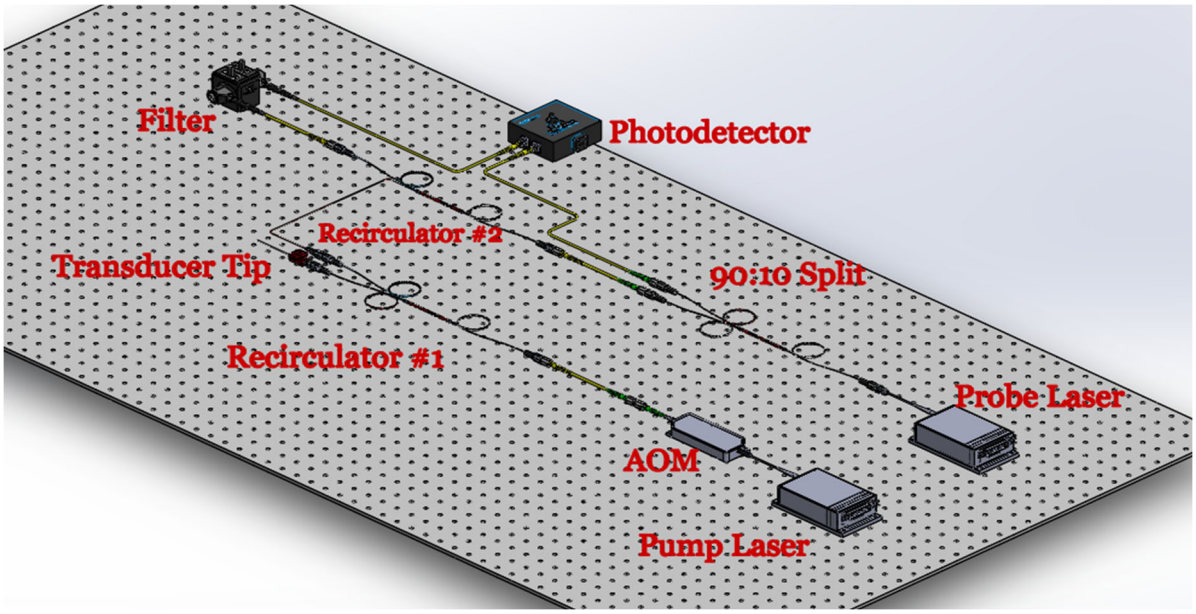

Figure 2.1: Schematic of the all-fiber FDTR system designed for this work. The system includes two fiber pigtailed pump and probe lasers to facilitate signal generation and probing as in free-space FDTR.

The system shown in Fig. 2.1 employs a fiber that has a gold transducer layer deposited on its surface (magnified in Fig. 2.2, below). In this arrangement, the fiber is put in contact with the material of interest. The pump and probe lasers both travel through a series of recirculators to the transducer and are reflected to the photodetector. The use of a recirculator allows for only the probe beam to travel back in the opposite direction and back to the photodetector, but the beam will still be color filtered to block any bleed-through light from the pump beam. The 90:10 fiber optic coupler passes 10% of the probe beam directly into the balanced photodiode in order to subtract any coherent noise from the probe laser cavity. The signal from the photodetector and AOM are coupled into a lock-in amplifier to determine the phase lag at the transducer surface, after which point our numerical model will be used to extract the underlying thermal properties from our measured data.

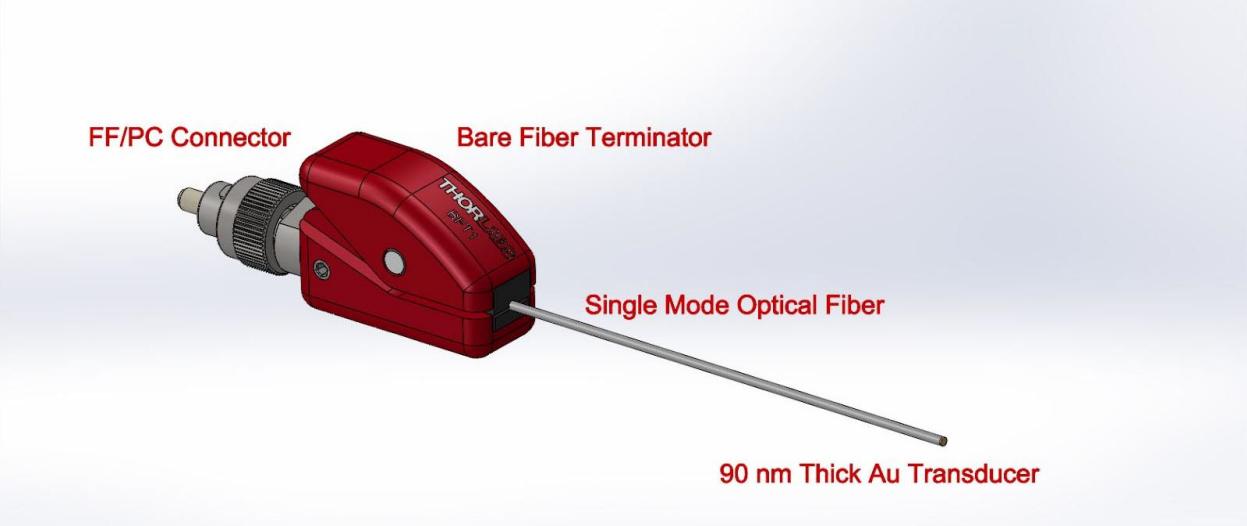

Figure 2.2: Novel Au/Ti alloy tipped bare fiber for contacting and measuring specimen. Dimensions of fiber and tip are exaggerated for visibility.

This novel probe tip brings with it two major areas of investigation for our research. First, there are new boundary conditions. Due to the small radius fiber tip,heat diffusion is constrained, rather than assumed infinite. Due to the contact between solids there is bi-directional heat flow,

both into the specimen, and back into the probe. Thus, the analytic solution can not be used and we must build a **numerical model.** Second, the **transducer coating** requirements, including: optical properties necessary to achieve a signal, adhesion sufficient for testing, and thermal properties to be sensitive to the specimens of interest.

3. Numerical Simulations

3. 1 Submerged in Fluid

This work required a numerical model to be integrated into our fitting technique for the fiber data. This is because the analytical model described earlier is only appropriate for a multilayer material system that is heated from above and is semi-infinite in the radial direction, as shown in Fig. 3.1.1 (a). The use of a fiber complicates the boundary conditions and results in both bi-directional heat flow and a confined radial geometry, as shown in Fig. 3.1.1 (b). This means that we must use a numerical model for the all fiber system.

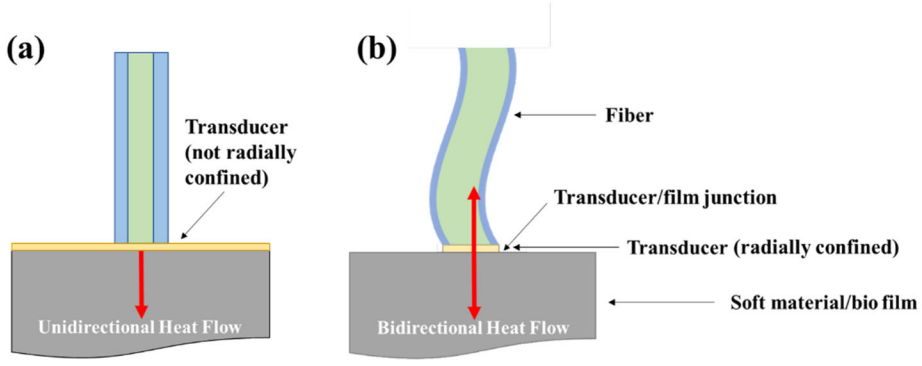

Figure 3.1.1: (a) Pump (blue) and probe (green) beams deposited onto transducer surface above a radially semi-infinite multilayer material, and (b) fiber with pump (blue) and probe (green) contained within its core, physically attached to a material system (pictured: soft material/bio film).

COMSOL coupled with MATLAB is used to build the model for this research. COMSOL is a Multiphysics FEA package that can solve the heat equation in the frequency domain, which is

simulated here. The frequency domain perturbation model is represented by equation 1,10, which is essentially Equation 1.1 after the Fourier Transform.

$$i\omega\rho C_p T + \nabla(-\kappa\nabla T) = Q + Q_p \tag{1.10}$$

In Eqn. 1.10, ω is the applied angular frequency, ρ is the material density, C_p is the specific heat capacity, T is the temperature (where ρ, C_p and T are assumed to be at constant pressure), Q is the average value of the heat load applied to the surface, and Q_p is the harmonic perturbation around Q [14].

Knowing that we would be curve fitting the data using MATLAB, we set the parameters as variables in such a manner that they would be able to be changed in COMSOL via the curve fitting routine. The first step of building the model in COMSOL is the geometry. Figure 3.1.2 displays the geometry from COMSOL showing the innermost radius which represents the core (the heated portion) and is set at 4 micrometers. The next represents the cladding, set at 121 micrometer thickness. The rest is water, which is set at a thickness of 300 micrometers. The zoomed in image in Figure 3.1.2 shows the geometry for the transducer. The transducer's radial thickness is that of the core, 4 micrometers. Its vertical thickness is 75 nanometers. Figure 3.1.2 is labeled for ease of understanding.

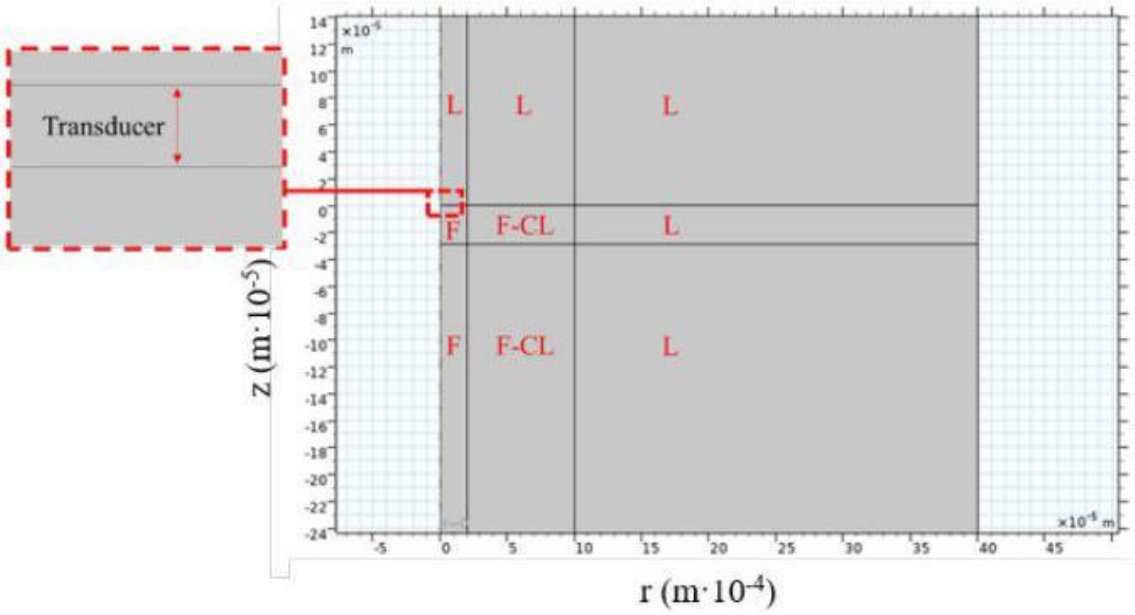

Figure 3.1.2: Model geometry figure retrieved from [14]. F is the fiber. L-CL is the fiber cladding. L is Liquid which is modeled as water. The transducer is too thin to be seen in the larger image and is thus zoomed in in the top left. The transducer is modeled as gold.

With the geometry declared we built a mesh with nodes to be analyzed. Using the validated mesh from [11] as reference. We used a rectangular mapped mesh where each domain has 50 elements in the radial direction and 25 elements in the z direction. Every element besides the transducer has an asymmetric gradation with an element ratio of 20. The transducer is symmetric with an element ratio of 20. These gradations are used to get more resolution near the boundaries where thermal gradients are expected to be larger. This leads to a Figure 3.1.3 from [14] shows the mesh on the geometry.

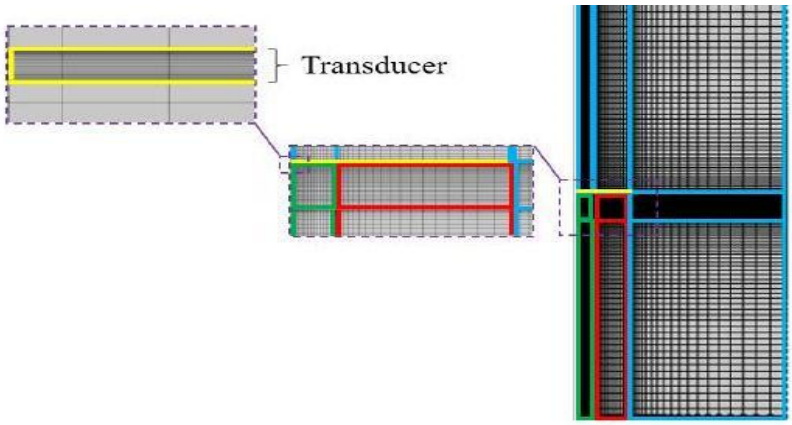

Figure 3.1.3: Mesh geometry retrieved from [14]. Node density is larger towards boundaries due to there being more information of interest at those areas. The mesh has asymmetric gradation aside from the transducer, which is symmetric due to our interest in properties of both of its edges.

Once the geometry and mesh is set we must input the material properties. The fiber is assumed to be equivalent to the properties of SiO_2 with a thermal conductivity of $1.4\ W\ m^{-1}\ K^{-1}$ and volumetric heat capacity of $1.85\ MJm^{-3}\ K^{-1}$. This is assumed to be the material of the core and cladding. The transducer is gold ($\kappa_{tr} = 220\ W\ m^{-1}\ K^{-1}$) and the environment is set to $\kappa = 0.598\ W\ m^{-1}\ K^{-1}$ to match that of water. Once the material properties were set, we utilized a frequency domain heat transfer equation ensuring proper boundary conditions were set throughout the interfaces in the fiber. The average transducer temperature is determined by integrating over the transducer assuming the probe has a Gaussian profile.

$$T_{avg} = \frac{4}{w_1^2}\int_0^{r_C} \quad exp\left(\frac{-2r^2}{w_1^2}\right) T(r) \cdot r dr \tag{11}$$

where r_C is the core radius and w_1 is the probe radius. The integral is evaluated in MATLAB and finally the phase lag is found using the real and imaginary parts of the average transducer temperature in the frequency domain just as in Equation 1.9,

$$\phi_{LI} = tan^{-1}\frac{J(T_{avg})}{R(T_{avg})} \tag{12}$$

This also required thermal contact relationships between surfaces. The thermal boundary conductance between the glass and water is set to 100 MW/m^{2}K, between the glass and gold is 150 MW/m^{2}K and gold and water 38 MW/m^{2}K. The remaining boundaries were thermally insulating.

With the model built, the goal of this study is to determine sensitivity. The conventional definition of sensitivity is,

$$S_p(\omega) = \frac{\partial \phi_{LI}(\omega)}{\partial ln(p)} \tag{13}$$

Where p is the parameter of interest. To evaluate sensitivity we perturb the parameter of interest by 1% in the MATLAB simulation and evaluate the difference in phase lag relative to the difference in ln(p)[14].

Figure 3.1.4 is an example of a sensitivity graph for one frequency sweep. This is a sample graph and does not include real data. For a given set of parameters one parameter perturbed at a time over a range of frequencies and the percent difference in the phase lag is observed. We take the maximum sensitivity of the sweep in order to find the sensitivity to our desired parameter.

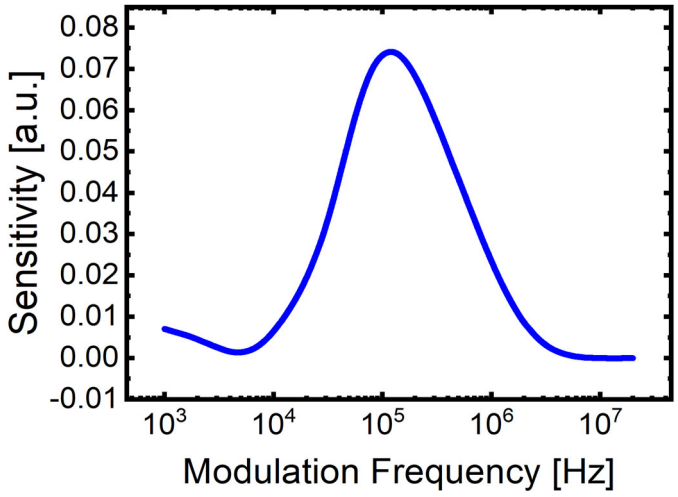

Figure 3.1.4: This is a sample sensitivity graph. It shows the sensitivity to the specimens conductivity through a frequency sweep. The point we care about on this graph is the peak. A value greater than zero anywhere in the sweep tells you that the sweep will successfully determine conductivity.

Figure 3.1.5 Gives a visual for some of the parameters that we will be adjusting and evaluating its changes effects on sensitivity.

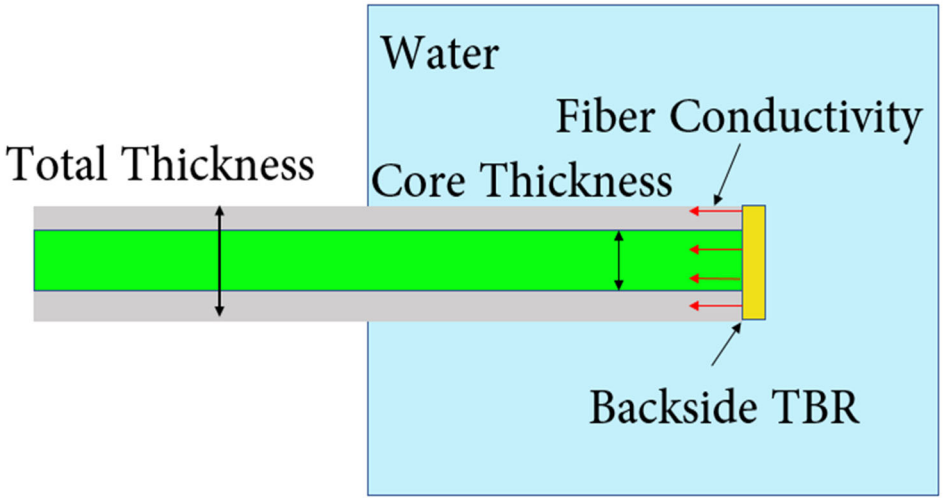

Figure 3.1.5: This gives an image to reference in regards to the parameters we will change to determine sensitivity.

3. 2 Results and Discussion for Submerged in Fluid Study

In order to confirm that a thermal characterization method is practical for a specific model and fitting routine, a sensitivity analysis must be performed. This analysis ensures that the set up is capable of measuring the material of interest.

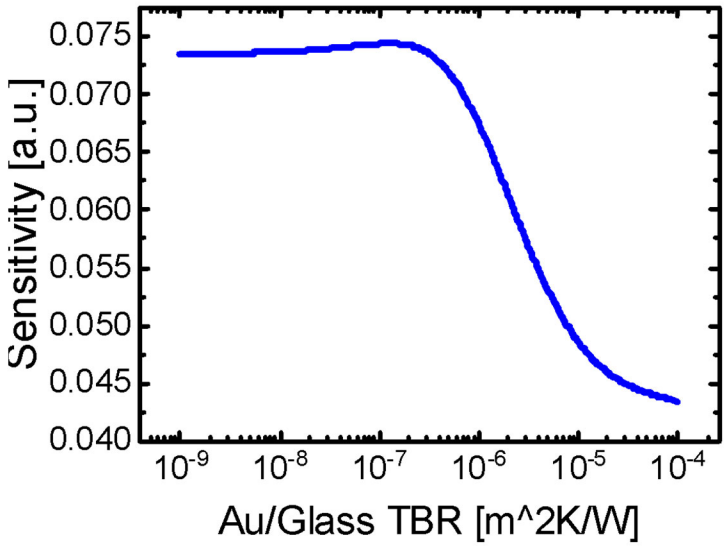

Figure 3.2.1: Sensitivity to Fluid conductivity with varying backside thermal boundary resistance

Figure 3.2.1 shows the relationship of sensitivity to the specimen conductivity with changing thermal boundary resistance between the gold transducer and glass. As thermal boundary resistance increases sensitivity decreases beginning to fall substantially at 10^{-6} m^2K/W. This makes sense and would correspond to poor adhesion of the transducer to the fiber [14].

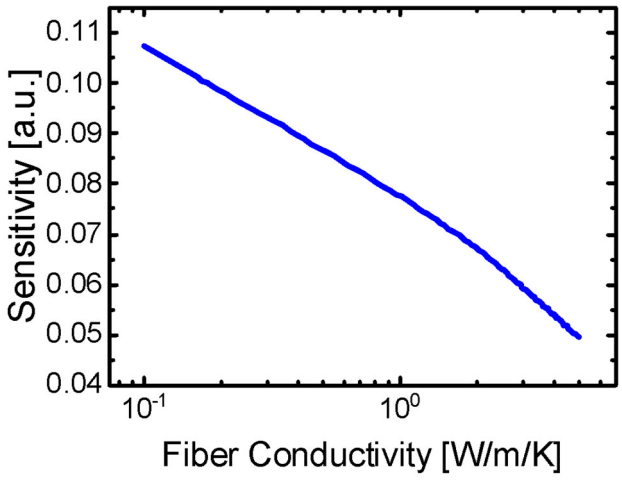

Figure 3.2.2: Sensitivity to Fluid conductivity with varying fiber conductivity

Figure 3.2.2 shows the relationship of sensitivity to the specimen conductivity with changing fiber conductivity of the fiber. If the fiber is more conductive, we are less sensitive to the specimen conductivity. This makes sense, because more heat is flowing back into the fiber, reducing our visibility of the specimen properties [14].

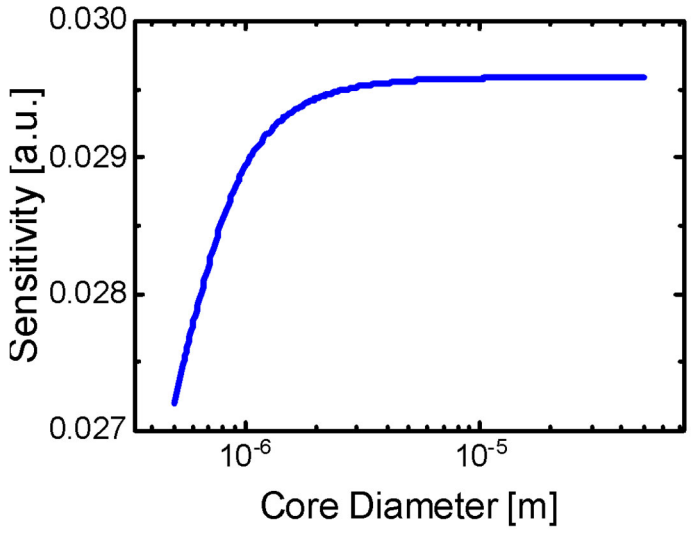

Figure 3.2.3: Sensitivity to Fluid conductivity with varying core diameter

Figure 3.2.3 shows the relationship of sensitivity to the specimen conductivity with changing core diameter. Sensitivity is relatively unchanged by core diameter as seen by a small change in magnitude.

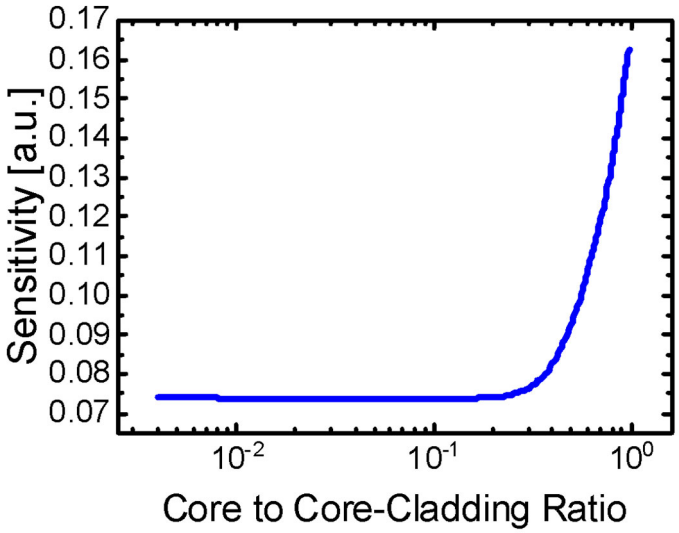

Figure 3.2.4: Sensitivity to Fluid conductivity with varying ratio between core thickness and total fiber thickness

Figure 3.2.4 shows the relationship of sensitivity to the ratio of core thickness to total core and cladding thickness. The closer the fiber is to being all core, the better the sensitivity. The ratio seems to need to be over 0.6 in order to be sensitive.

These sensitivities are useful in understanding the importance of parameters of the fiber tip. As part of this work, we determined the impact of different parameters on the sensitivity to measuring a liquid near the conductivity of water. Sensitivity to the thermal properties of the sample also improves with decreasing fiber thermal conductivity This makes sense due to the parallel paths for heat transfer; in the case of a thermally insulating fiber, heat is prevented from flowing back into the system. The core diameter does not have much bearing on the sensitivity in this particular application. It might be more important to consider in the measurement of cells and instances where the probe is not dipped in a fluid. Finally, to be sensitive to the material, it is better that over

60% of the fiber is made up of the core, with 40% or less being the cladding. This is likely due to the elimination of a third parallel channel for heat transport (from the transducer into the cladding). Optimizing these parameters, along with those cited in ref. [14], allows us to select or design a fiber tip with the ability to measure liquids having thermal conductivities similar to that of water. Given the results reported in ref. [6], it is reasonable to expect that a fiber probe would work well to characterize aqueous material systems using an optical pump-probe thermoreflectance experiment. These studies validate that such fibers are compatible with FDTR, allowing for the future development of an all-fiber thermoreflectance system having the mobility necessary for materials characterization in extreme environments (e.g., environmental chambers).

3.3 Particle Contact

As part of this work, we also interrogate the expected measurement sensitivity to the thermal properties of particles in contact with the fiber probe. This could have applications in testing cells or in particle bed 3D printing and is another way that we could learn about the potential capabilities and needs of our system in this alternate domain from the submerged liquid.

Knowing that including a particle would add a round geometry we had to modify the meshing approach. For the previous model, we employed a rectangular mapped mesh. For the particle mesh it was apparent that a physics controlled triangular mesh would be necessary due to the round geometry. This necessitated a mesh independence study to ensure that we still had reliable results. The meshes used are seen in Figure 3.10 and the details about the meshes are in Table 1.

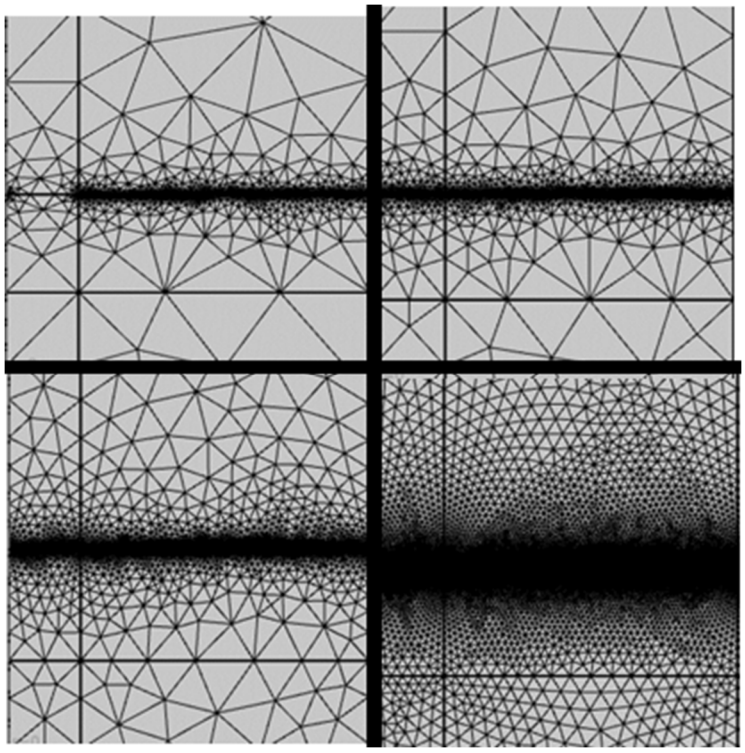

Figure 3.3.1: These are the four meshes used in the study. Upper left: Extra Coarse, Upper right: Coarser, Lower left: Normal, Lower right: Extremely Fine. Notice that the Extra Coarse has low density around the transducer.

Coarseness	Domain Elements	Boundary Elements	Computational Time [s]
Extra Coarse	59174	7435	91
Coarser	81038	7837	122
Normal	109774	7913	169
Extremely Fine	276164	8497	406

Table 1: Table 1 displays the size of each mesh and the amount of time it takes to compute the solution with that mesh.

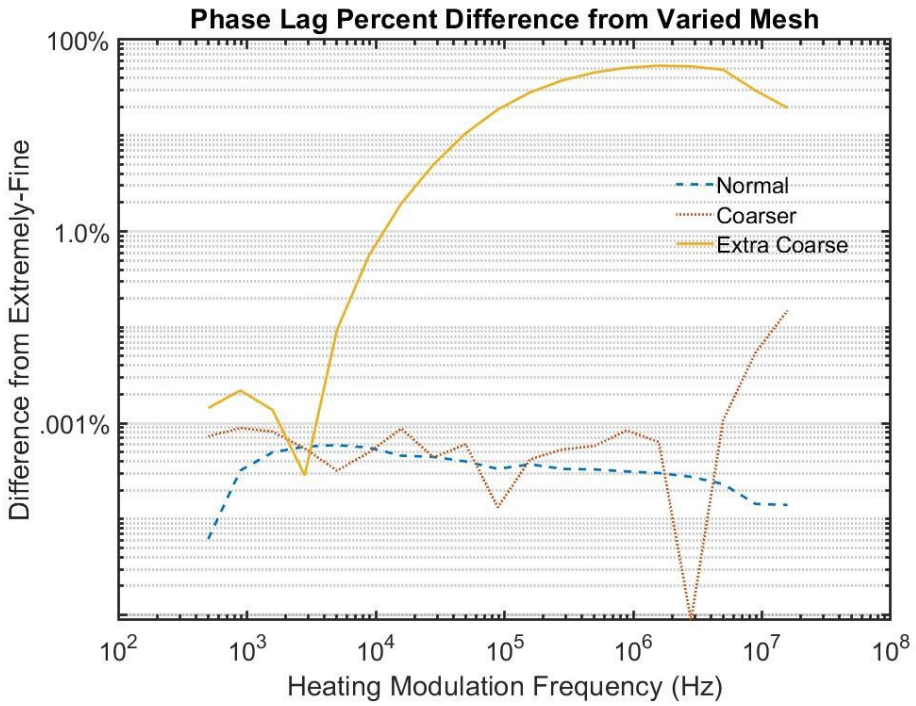

Figure 3.3.2: Above, we compare the phase lag of each mesh to the extremely fine mesh. The percent difference is insignificant for normal and coarser, but is considerable for the extra coarse mesh.

The percent difference in phase lag between the meshes and the reference, extremely fine, mesh is seen in Figure 3.3.2. Both the normal and coarse mesh have below .001% difference through most of the frequency sweep. A slight jump is seen in the 'coarser' mesh data in the higher frequencies. This is when the heat does not penetrate as deep and thus may be more reliant on a finer mesh near the transducer. The percent difference at the highest point for the 'coarser' is still below .02%. The 'extra coarse' mesh saw significant deviation from the 'extremely fine' reaching nearly a 100% difference in phase lag results. In Figure 3.3.2 it can be seen that the mesh is not as dense around the transducer like the other meshes were. This is likely the source of the error and means that a 'coarse' mesh is the lowest resolution that we should use to allow for efficient running of analysis.

After verifying that a physics mesh could be used and building our mesh we could begin testing for the particle sensitivity and building our model. This utilizes the same base as the previous model, however a particle has been added on the surface of the transducer. To facilitate this study, we changed the surrounding fluid to have the properties of air. The particle addition and mesh can be seen in Figure 3.3.3.

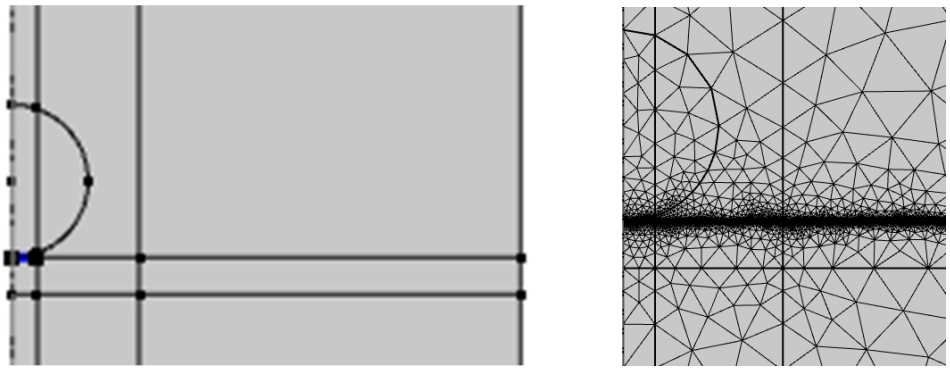

Figure 3.3.3 On the left, you can see the particle added to the system described earlier. On the right is the triangular mesh applied after the mesh study.

First, we attempted to use liquid water and found that its relatively high conductivity led to inconclusive results with no distinguishable relationships. This is likely due to the heat flowing into the water rather than the particle of interest. We considered an insulated boundary condition or applying a contact resistance within COMSOL, but instead settled with changing the fluid properties to that of air. This is a low conductivity gas that produces the effect of a contact resistance between the transducer and edges of the particle. We added parameters for the model to be able to adjust the radius, conductivity, density, and heat capacity. We created the radius parameter such that the radius would change but the edge would remain tangent to the surface of the transducer, contacting in the center. We then used the same sensitivity concepts elaborated in the last section to analyze this particle model. Table 2 below shows the default parameters used for the sensitivity study.

Parameter	Transducer Width [m]	Particle Radius [m]	$K_{Transducer}$ [W/m/K]	K_{air} [W/m/K]	K_{fiber} [W/m/K]	$K_{particle}$ [W/m/K]
Default Value	20e-6	4e-6	220	.02-.06	1.4	100

Table 2: Displays the default parameters used for the sensitivity study carried out below

3.4 Results and Discussion for Particle Study

We preformed the particle sensitivity study considering a variety of parameters.

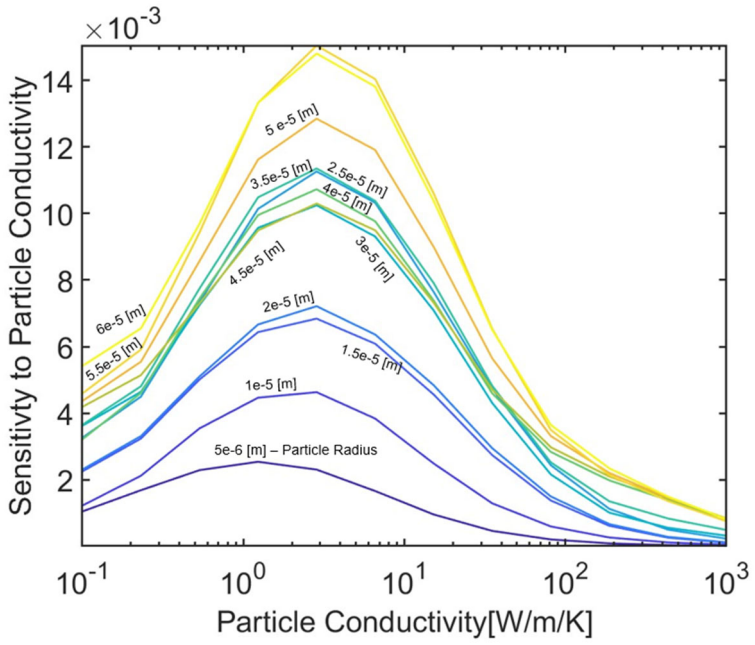

Figure 3.4.1: Sensitivity to particle conductivity with varying core diameter and particle size

Figure 3.4.1 displays the sensitivity for particle conductivity for both change in particle conductivity and change in particle size. From the particle conductivity sweep, through all the particle sizes, there is a specific particle conductivity that is most sensitive, after which, it tapers to zero. This is likely due to the heat reaching the thermal boundary of the sphere faster, resulting in a higher proportion of the heat going back into the fiber.

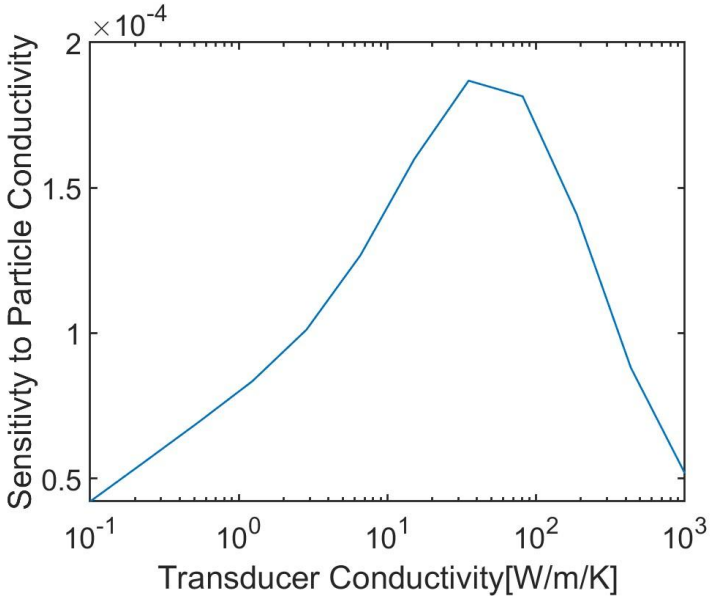

Figure 3.4.2: Sensitivity to particle conductivity with varying transducer conductivity

Figure 3.4.2 shows the sensitivity to particle conductivity with a change in transducer conductivity. The optimal transducer conductivity, with the particle at 100 W/mK is around 220 W/mK which is coincidentally close to the conductivity of gold which we use as the default for this study. This may change with other particle conductivities, but it shows that there is an optimal transducer conductivity for each measurement.

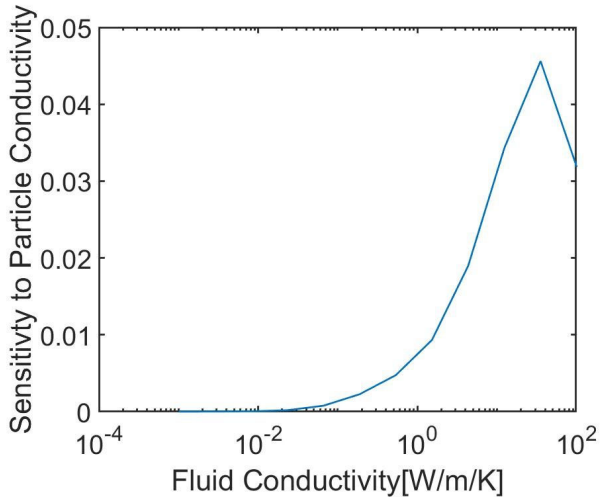

Figure 3.4.3: Sensitivity to particle conductivity with varying fluid conductivity

The reaction of sensitivity to change in fluid conductivity is seen above in Figure 3.4.3 . At low fluid conductivities the heat likely cannot cross the air boundary to contact the particle. Over a certain threshold fluid conductivity, the sensitivity begins to rise as the heat can travel to the particle. Once the fluid's thermal conductivity surpasses a threshold, the fluid is primarily dissipating the heat.

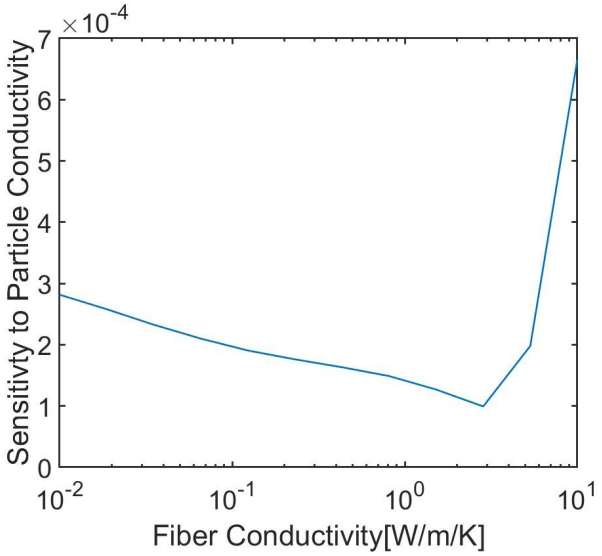

Figure 3.4.4: Sensitivity to particle conductivity with varying fiber conductivity

The impact of the fiber's thermal conductivity on the sensitivity to the particle's thermal conductivity is seen in Figure 3.4.4. As fiber conductivity increases, the sensitivity decreases until a threshold after which it begins rising. This rise is likely due to the fiber no longer acting as thermally resistive in the circuit.

These graphs and findings help us to understand the ability to test the thermal properties of a particle contacting the middle of our fiber tip. These trends will help us in designing and testing our transducer tip as well as understand what type of materials we will be able to test and in what kind of environments.

In tandem with the experimental system, we will continue refining and studying our numerical model. This will ensure faster results and troubleshooting of the system once we are able to take readings. While the particle setup was a good start, we would like to test how the contact location of the particle affects readings, multiple particle effects, and potentially different particle shapes.

4. Transducer Studies

4.1 Early work

To verify that this will not prohibit the development of our all-fiber system, we measured preliminary thermal data for the Au/Ti films on BK7 glass with varying mass fractions of Ti (from 0% to 10%) on the Free Space FDTR system. All three films produced a sufficient thermoreflectance signal for measurement of the phase lag, as shown in Fig. 4.1.1. Thermal conductivity decreases significantly with the addition of Ti principally due to defect scattering in the alloy, as shown in Fig. 4.1.2. We expect this benefits the measurement due to limited thermal spreading in the Au layer, which pushes more heat into surrounding low thermal conductivity materials (in the range of most common biological materials).

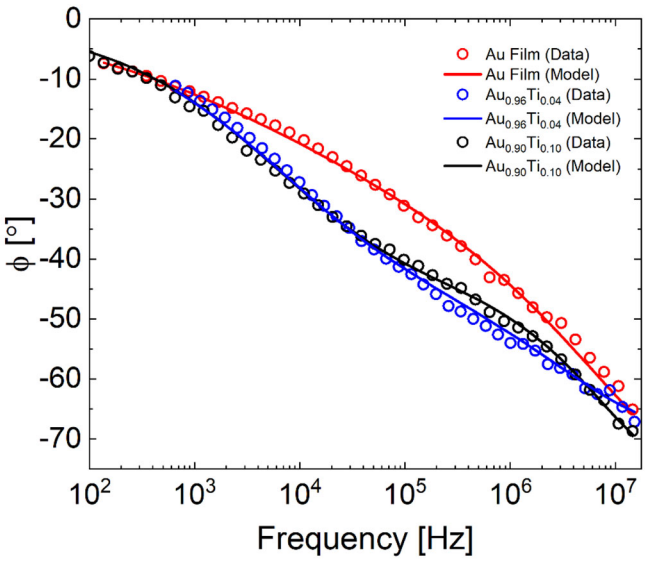

Fig. 4.1.1: Phase lag (ϕ) over a range of frequencies for Au/Ti alloys ranging from 0% Ti to 10% Ti.

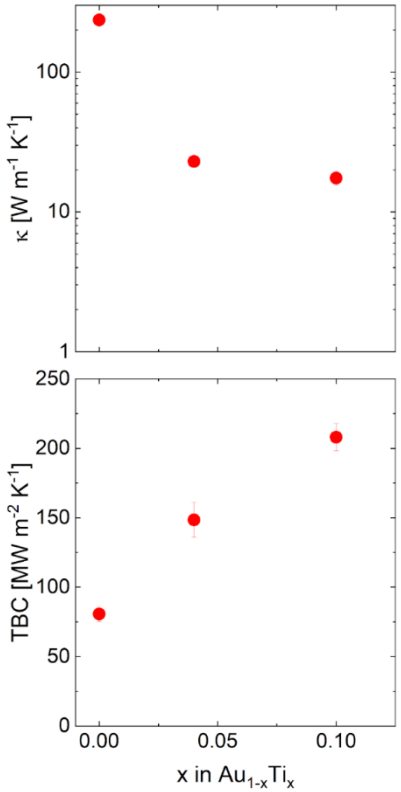

Figure 4.1.2: Thermal conductivity (κ) and Thermal Boundary Conductance (TBC) for Au/Ti alloy films ranging from 0% to 10% Ti.

Figure 4.1.2 also indicates that the thermal boundary conductance at the transducer/glass interface (i.e., how well heat moves between the transducer and the glass) increases with increasing mass fraction of Ti. This provides us with initial evidence that suggests the Au/Ti film adheres well to the substrate. Generally, values of TBC > 100 $MW/m^2 \cdot K$ indicate sufficient adhesion. Thus, a relatively low mass fraction of Ti is suitable for the Au/Ti transducer. After this preliminary study using FDTR, we executed further transducer studies using SSTR and other experimental methods, detailed below.

4.2 Making Samples

While the modeling assists in understanding what transducer properties are useful in measuring certain materials, it is also necessary to do testing on the potential alloys for use with the transducer tip. The challenge of the transducer tip is that while gold is an appropriate transducer due to its thermoreflectance properties, it does not adhere to glass by itself. It is susceptible to the environment and thus contact with a sample or fluid may damage the transducer, rendering it ineffective. In free space FDTR, a typical procedure for a 100nm film transducer would be to coat the substrate in a layer of titanium 10nm thick and then a layer of gold 90nm thick. The titanium acts as an adhesion layer between the surfaces, which prevents delamination of the gold transducer. The potential problem with using this technique on the fiber probe is that having a layer of Ti between the Au and glass could prevent an adequate thermoreflectance signal due to the Ti reflecting the light before it reaches the Au. This relationship and balance necessitates further study on the potential transducer arrangement. Thus, in this Trident project we undertook experiments to study potential transducer coatings.

The first step we took was coating fibers with our collaborator, Dr. Adam Wilson at the Army Research Lab. We used their AJA ATC Flagship co-sputtering system to coat the fibers and a

glass slide so that we could test it using the free space FDTR system. The co-sputter machine and slide coating can be seen in figure.

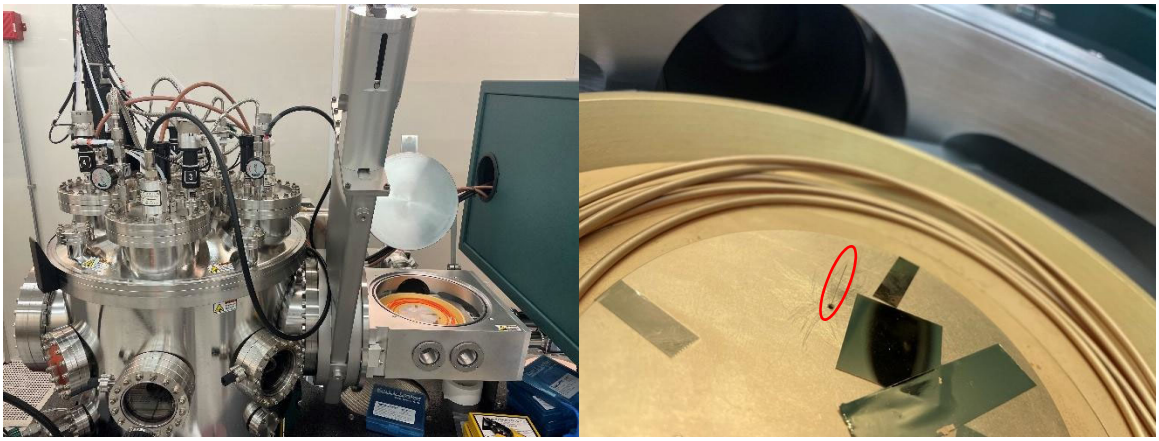

Figure 4.2.1: On the left is the cosputtering chamber with the uncoated fiber and slide on the tray. On the right is the completed specimen with the fiber sticking out of the hole (circled in red), and a slide coated at the same time.

Using this cosputtering chamber we made four pairs of fiber/slide samples: Gold, an alloy with 5% Ti 95% Au, an alloy with 10% Ti 90% Gold and a sample with 10nm layer of Ti and 90nm Au. These slides allow us to use other testing methods to test the same arrangements of materials that we deposited on the fibers.

In addition to the cosputtered samples, we used an Electron-beam (E-beam) depositing method available at the academy to make a series of bilayer samples with different thicknesses of Ti. We coated three substrates, BK7 glass, sapphire, and X-cut quartz with a specific thickness of Ti (0, 2, 5, 10, 25, and 40 nm) and 80nm of Au. At this stage, we have only performed a full analysis on the BK7 glass as it was the closest to our fiber material. This provides us with a sample set through which to evaluate a Ti adhesion layer rather than Ti alloy for the transducer.

4.3 Characterizing Samples

To properly characterize the samples, we first use a Veeco Dektak 150 to measure the thickness of material layer, as seen in Figure 4.3.1.

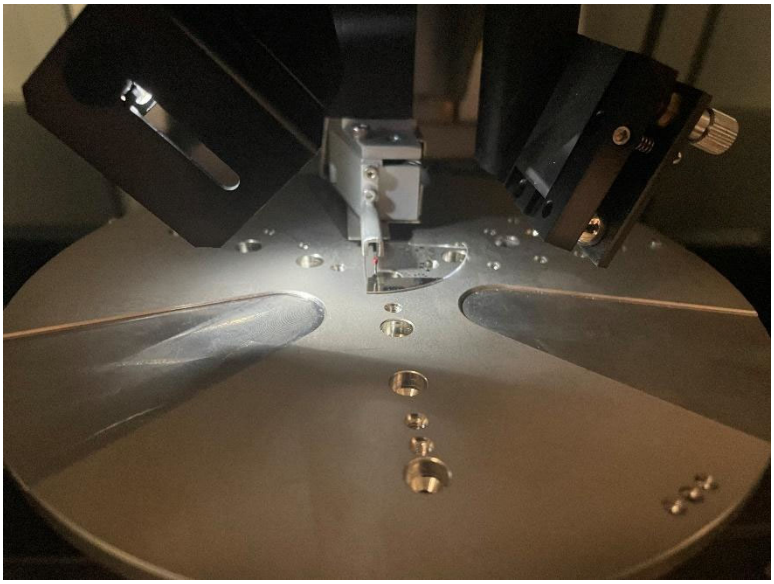

Figure 4.3.1: The profilometer drops the probe onto the sample, then drags for a set difference and measures the depth of the probe to measure the profile of the surface of the sample. We take the difference between the height when it is on the coated portion and an uncoated portion.

The thickness is useful in modeling the thermal properties of our samples, which is described further in a later section. In addition to the thickness we determined the electrical conductivity of each sample using a four-point probe (4pp). The apparatus measures the resistance with four in line probes to determine the film conductivity of the samples. We executed the 4pp experiment using a Signatone S-302 seen in Figure 4.3.2. Through inducing a voltage and reading current, the probes are used to determine electrical resistance in the sample. Using the measured thickness, we convert the resistance into film resistance and then take the inverse to get electrical

conductivity. Using the Wiedemann-Franz Law, we relate electrical conductivity to thermal conductivity, a characteristic of interest in our samples.

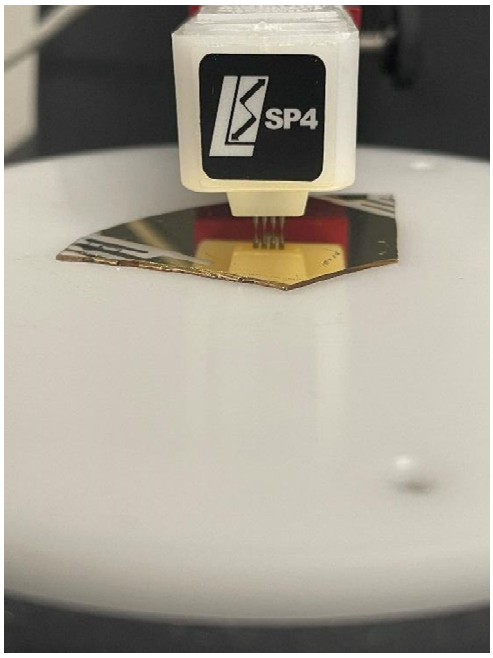

Figure 4.3.2: Above is a four-point probe testing set up. The two outboard probes induce a voltage and the inside two probes read current thus determining the resistance in that line.

In addition to thermal conductivity and thickness, we use the free space system to measure the reflectivity of the samples. We do this by measuring the power of the laser immediately before and after contacting the sample. The percentage of the incident power that reflected is recorded as the reflectivity. For each property on each sample, multiple trials are executed for each experimental method and the average is taken.

In addition to these experiments, we ran a simple scratch test to get a qualitative of the adhesion of the transducer to their underlying substrate. To accomplish this, we wiped the surface of the sample with a chem wipe, rubber tweezers, then hard tweezers. The results from these characterization efforts are found in Table 4.

Deposit method	Sample	Thickness [nm]	κ [W/mK]	ρ (front)	ρ (back)
Cosputter	Au	101.4	190.2	.686	.612
Cosputter	Au 95% Ti 5% Alloy	137.4	12.14	.585	.514
Cosputter	Au 90% Ti 10% Alloy	128	5.75	.62	.508
Cosputter	Au 5nm Ti Layer	92.5	188.73	.728	.275
E-Beam	Au	79.2	220.39	-	.667
E-Beam	Au 2nm Ti Layer	84	212.18	-	.584
E-Beam	Au 5nm Ti Layer	89.2	200.36	-	.389
E-Beam	Au 10nm Ti Layer	91.5	183.91	-	.388
E-Beam	Au 25nm Ti Layer	101.2	166.74	-	.403
E-Beam	Au 40 nm Ti Layer	118	139.00	-	.415

Table 4: This table displays the results of the Transducer characterization study

4.4 Thermoreflectance measurements

With these properties taken, we began testing our transducer samples using our FDTR system. We utilized low frequency sweeps used the math below to relate the probe signal change to specific physical characteristics by relating the slopes between several samples. Here, we use reflectance relationships to determine the thermoreflectance of our samples.

$$\frac{\Delta V}{V} = \frac{\Delta R}{R} = \left(\frac{1}{R}\frac{\partial R}{\partial T}\right)\Delta T = \beta \Delta T \tag{2.1}$$

ΔV represents the magnitude of the oscillating thermoreflectance signal and V represents the flat, steady reflected probe photodetector signal. This relationship is equivalent to the change in reflectivity (ΔR/R) with the modulated heat over the reflectivity of the sample. Finally, this percent change in reflectivity is equivalent to the thermoreflectance coefficient β times the change in temperature.

$$\left(\frac{\Delta V}{V}\right) = m\Delta P \tag{2.2}$$

For the method we use a graph with the y axis of ΔV/V and an x axis of pump power, ΔP. This provides a linear relationship with the slope of m above and we can derive properties from this slope as seen in Figure 4.4.1 taken from [15].

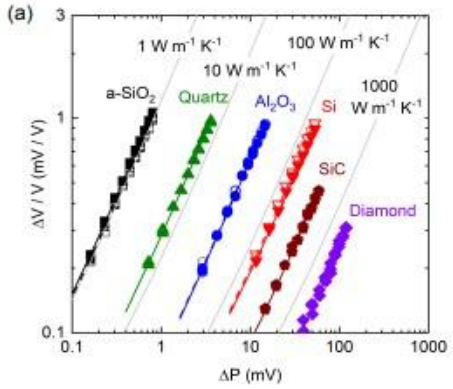

Figure 4.4.1: Above is an example graph for SSTR found in [15]. It compares several substrates with the same transducer, scanned in the same set up. The slopes here were used to extract the conductivity of the sample.

$$\left(\frac{\Delta V}{V \Delta P}\right) = m = \beta * f(\kappa, t) * C \tag{2.3}$$

Here we use our slope to extract the coefficient of thermoreflectance. The cosputtered and the E-beam samples all have the same substrate. The difference is the properties of the transducer. Thus, the slope consists of the thermoreflectance coefficient, some function of the thickness and conductivity of the transducer, and a correction factor that accounts for other constant quantities in our experimental set up.

$$C = \frac{\beta_{Au} * f(\kappa_{Au}, t_{Au})}{m_{Au}} \tag{2.4}$$

To determine the correction factor, we had to start with a transducer of known properties. In this case each the cosputter and E-beam samples had a pure gold sample that was effectively the control. Gold has a known coefficient of thermoreflectance of 2.6e-4 which we determined using [16[and the figure below.

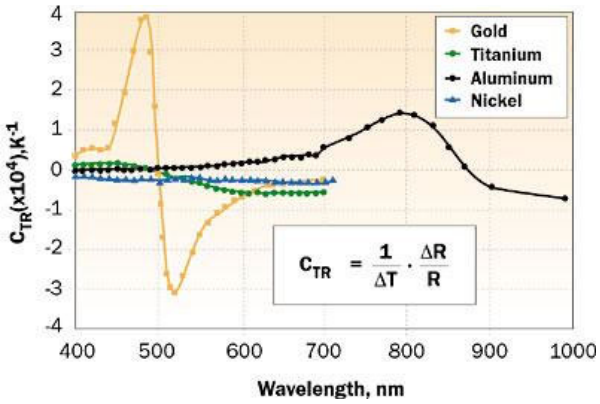

Figure 4.4.2: Above is the thermoreflectance coefficient for several potential substrate materials over a range of wavelengths. For the low frequency study we used the thermoreflectance coefficient at 532 nm the wavelength of our probe laser as determined from the graph above.

The other parameter that we needed to solve for was the dependence of the temperature of the sample on thickness and thermal conductivity of the transducer. To accomplish this, we designed a bilayer study in COMSOL, which solved for the temperature at the surface at various thickness and conductivity values of the film on top of a glass substrate. This resulted in a surface for each sample set that we were able to interpolate for the specific thickness and conductivity of the samples, and use in our data processing. The surfaces and interpolated points are seen in figure 4.4.3.

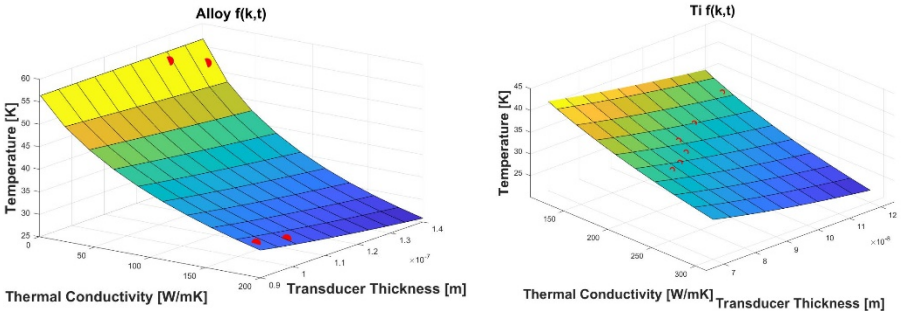

Figure 4.4.3: Above are the surface functions for each of the sample sets. The marks on the graph are interpolated for the measured thickness and conductivity of the sample. The function result for gold is used as the control and then we are able to solve the remaining samples.

To test the samples, we took each specimen and ran them through several low frequency sweeps on the FDTR system at several pump powers. We probed the Ti series through the glass, as we were interested in the internal fiber signal that may result from the layering. When analyzing the different frequency results, we found that as the frequency increased, the data became less linear, which is consistent with the low frequency methodology. This can be seen in the figure below.

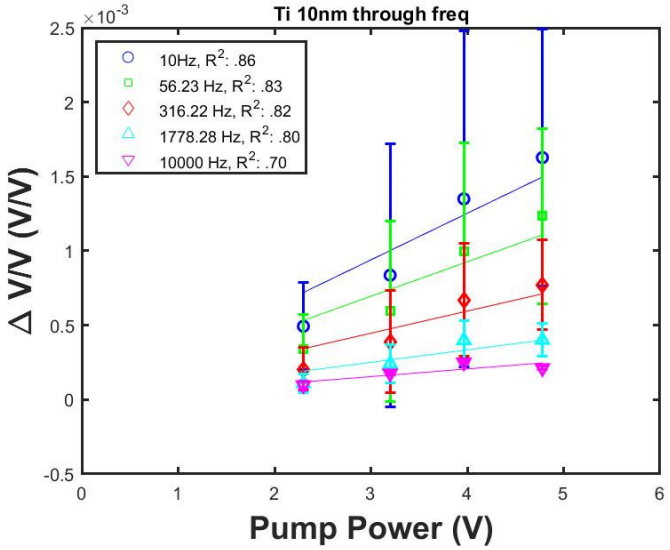

Figure 4.4.4: Above is the 10 nm E-beam Ti sample. The data demonstrates that a higher frequency leads to a lower magnitude signal and is less linear as demonstrated by the decreasing R^2 value.

Therefore, we used power sweeps over the lower frequency to characterize the two sets of samples. The resulting graphs from the study can be seen below in figures 4.4.5 and 4.4.6.

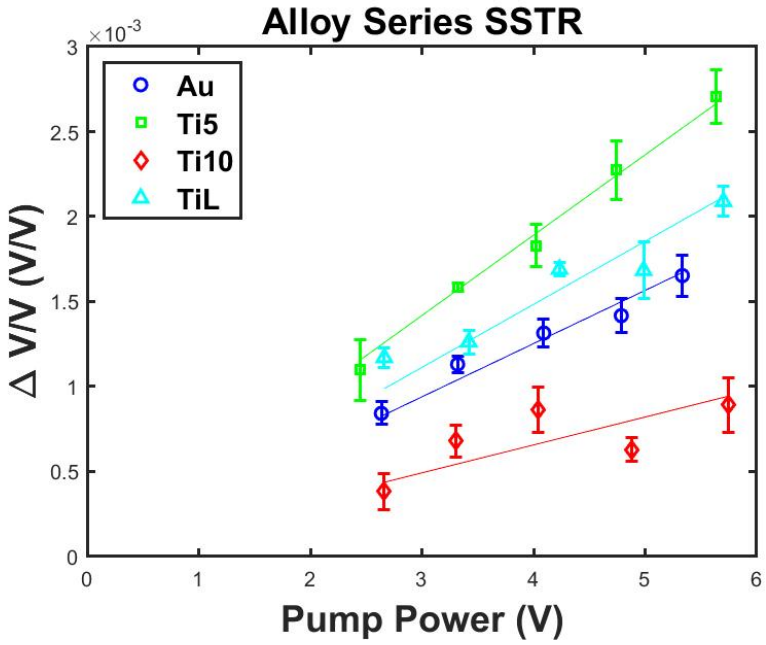

Figure 4.4.5: The cosputtered alloy sample results for the power sweeps

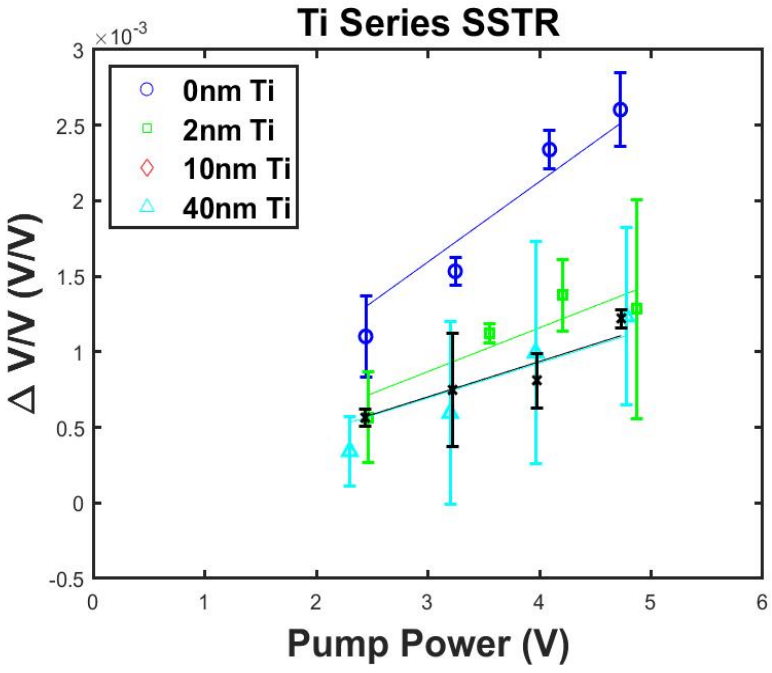

Figure 4.4.6: The E-beam Ti layer sample results for the power sweeps

The table below displays the results from the transducer study.

Deposit method	Sample	β [10^4 K^{-1}]	κ [W/mK]	ρ (front)	ρ (back)
Cosputter	Au	2.60±.13	190.2	.686	.612
Cosputter	Au 95% Ti 5% Alloy	2.27±.07	12.14	.585	.514
Cosputter	Au 90% Ti 10% Alloy	.754±.17	5.75	.62	.508
Cosputter	Au 5nm Ti Layer	2.96±.25	188.73	.728	.275
E-Beam	Au	2.6± .27	220.39	-	.667
E-Beam	Au 2nm Ti Layer	1.43±.2	212.18	-	.584
E-Beam	Au 5nm Ti Layer	-	200.36	-	.389
E-Beam	Au 10nm Ti Layer	1.12±.27	183.91	-	.388
E-Beam	Au 25nm Ti Layer	-	166.74	-	.403
E-Beam	Au 40 nm Ti Layer	1.12±.07	139.00	-	.415

Table 5: This table displays the results of the Transducer thermoreflectance study

With increased Ti content in the alloy for the cosputtered sample, we observe a drop in the thermoreflectance coefficient. With the increased Ti thickness for the E-beam samples, we see an initial drop in thermoreflectance coefficient. After a certain thickness, the thermoreflectance coefficient becomes dominated by the Ti and stops decreasing. For the adhesion test, the gold transducer for both the cosputtered and E-beam were removed by the chem wipe, the alloys were both able to be removed by the rubber tweezers, and the Ti layer samples, even as low as 2mm were not able to e removed by any implement, including the metal tweezers.

5. Fiber system

5.1 System construction

After beginning efforts on constructing the all fiber system we ran into some difficulty. The pump laser (Coherent Sapphire 532 nm Fiber Pigtail Laser) and probe laser (Coherent Sapphire 488 nm Fiber Pigtail Laser) referenced above had tips that we were not able to couple with the rest of our system. After unpacking them and getting them running, we were getting good power output. However, after connecting into a single patch cable we were observing substantial losses (18mW reduced to .7 mw). After significant troubleshooting and communication with the company we found that due to the high power of the fiber laser, it was equipped with an end cap that diffused the laser shown in Fig. 5.1.1. This explained why the power readings were good, but it could not be connected into the fibers in our system.

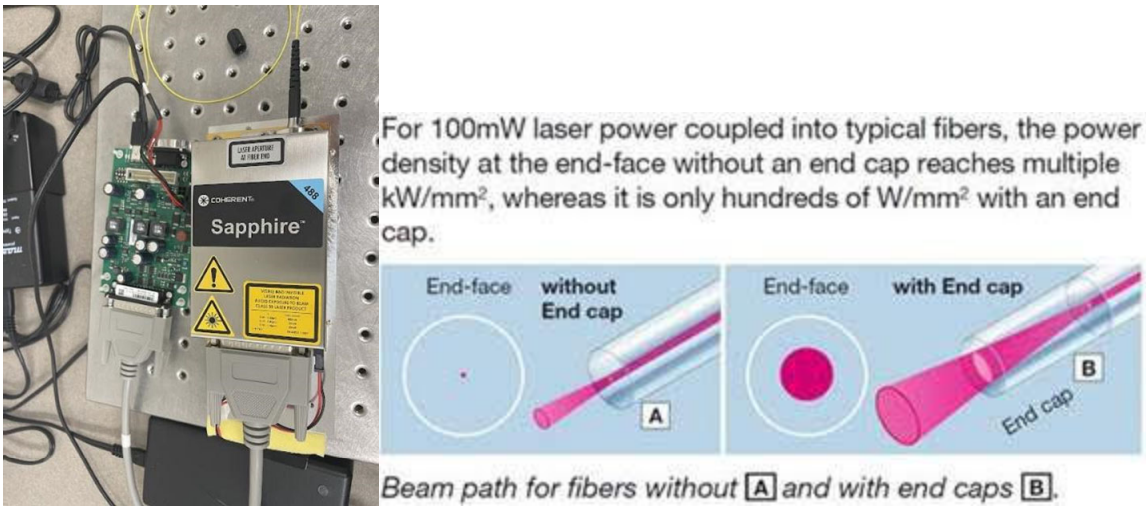

Figure 5.1.1: On the left is the Coherent sapphire pigtail laser that we intended to use for the application. After much trouble shooting and communication with the company, they provided the image on the right detailing the diffuse end cap which prevents us from pairing into the system.

After understanding this issue, we moved away from the sapphire lasers and were able to use separate drivers for lower powered lasers that could be integrated into the system. This did not have the significant losses that we had before, which enabled us to set up the system according to the schematic and test the components as seen in Fig. 5.1.2.

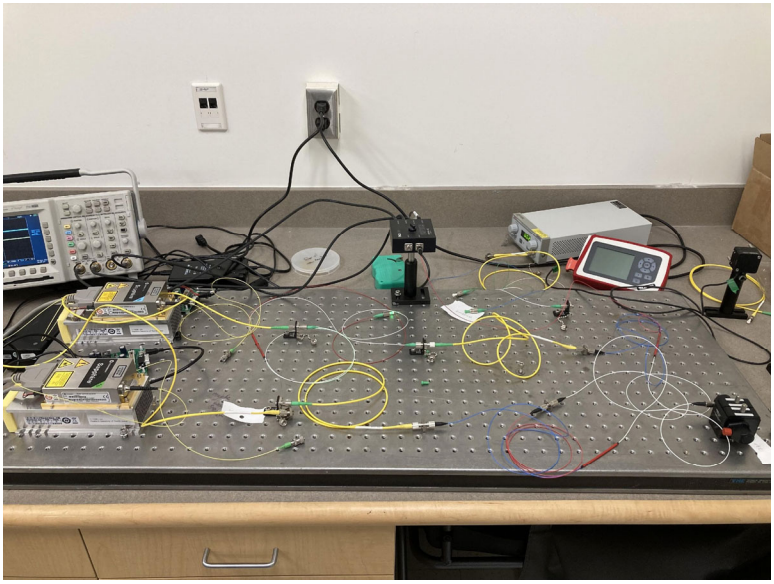

Figure 5.1.2: Above is the fiber system as seen in the earlier CAD model constructed in real life. While the pump and AOM are not currently installed, the probe path is completely built and was tested.

Component	Initial output	Patch#1	90:10 90	90:10 10	Patch#2	Circulator 1	Probe
Power (mW)	13.9	11.3	7.8	1.15	7.3	6.9	6.3

Component	Circulator 1	Circulator 2	Probe input
Power (mW)	3.2	3.84	4.34

Table 6: This table displays measurements taken through the probe laser's path. The top table shows power through the system going from the laser to the probe. The bottom table shows the power going from the probe back through the circulators. The bottom table is meant to ensure that light going into the probe (in the future reflected by the transducer) would go back through the system properly.

The results in Table 6 show the power of probe light moving through the system, and indicate that while our fiber system does not have significant losses, it is effective at getting the laser energy from the input to the probe. The second table shows that reflected probe light travels back through the system.

After determining that light could successfully travel both ways in the system, we wanted to observe how a reflection may be observable in the system. We did this by outfitting our in-line filter mount with a mirror to reflect some of the probe output light back through to replicate part of the effect that might occur when it hits the transducer. We routed this light into a balanced photodetector and read it with an oscilloscope. The maximum power that the photodetector could read without overloading is 1.8mW which as seen by the data above is achievable in the system even with some losses. The power without the mirror vs with the mirror added was noticeably different which provided confidence that we were successfully returning light from our transducer. The mirror set up is shown on Fig. 5.1.2 on the next page.

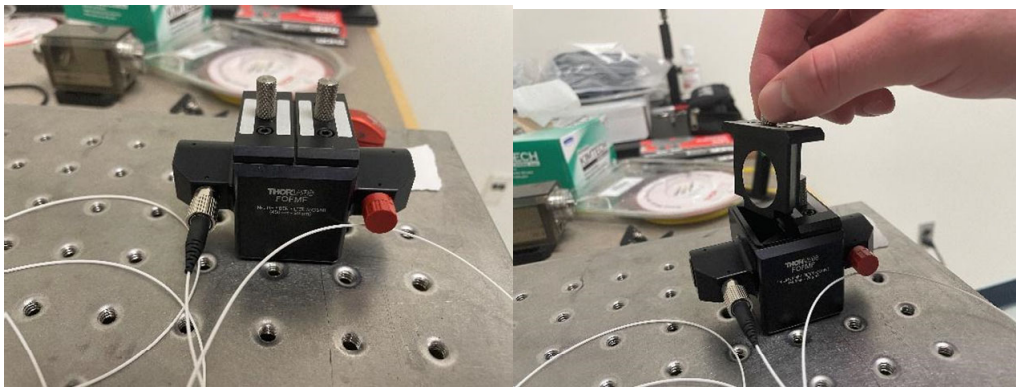

Figure 5.1.2: Above is an in-line filter mount that we will be using to filter the pump and probe light before the photodetector. We installed a mirror rather than a filter in order to check if reflections are observable by the system.

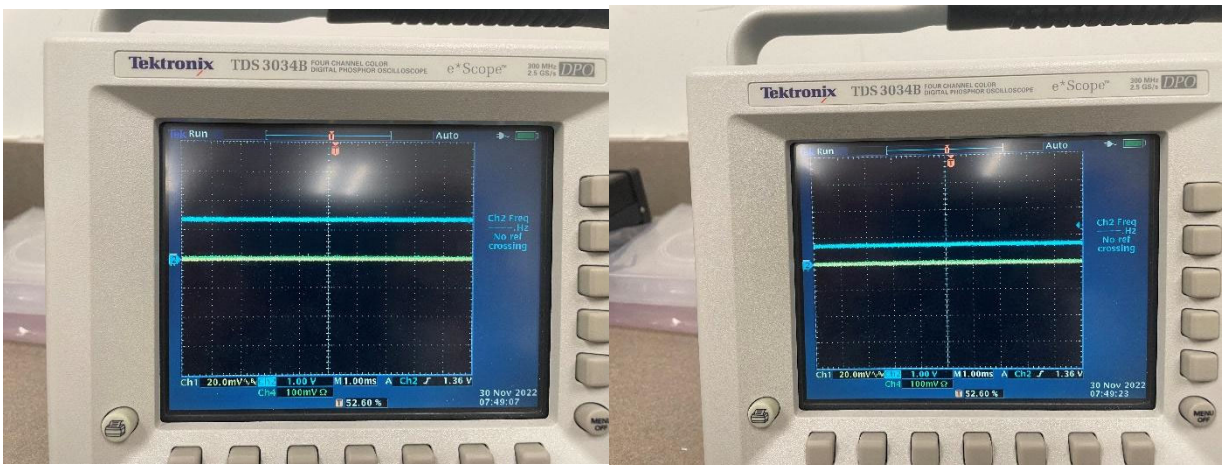

Figure 5.1.3: On the left is the photodetector reading with the mirror in the mount. It reads 1.36V. On the right is with the mirror out and reads 720 mV. The trigger is left at the initial reading to observe the difference. It was clear the reflections could be seen in the system.

Figure 5.1.3 above shows the readings from the photodetector before and after the mirror is put in. This experiment showed that we could successfully observe reflections at the probe tip using our set up.

Once we had validated that light traveled through the system correctly, we moved forward with coupling a free space pump into the fiber system. Stripping the fiber, and using the apparatus

below, we were able to pair a modulated pump signal into our fiber system. Aside from this free space modulated laser paired into the fiber, the rest of the system was fiber based.

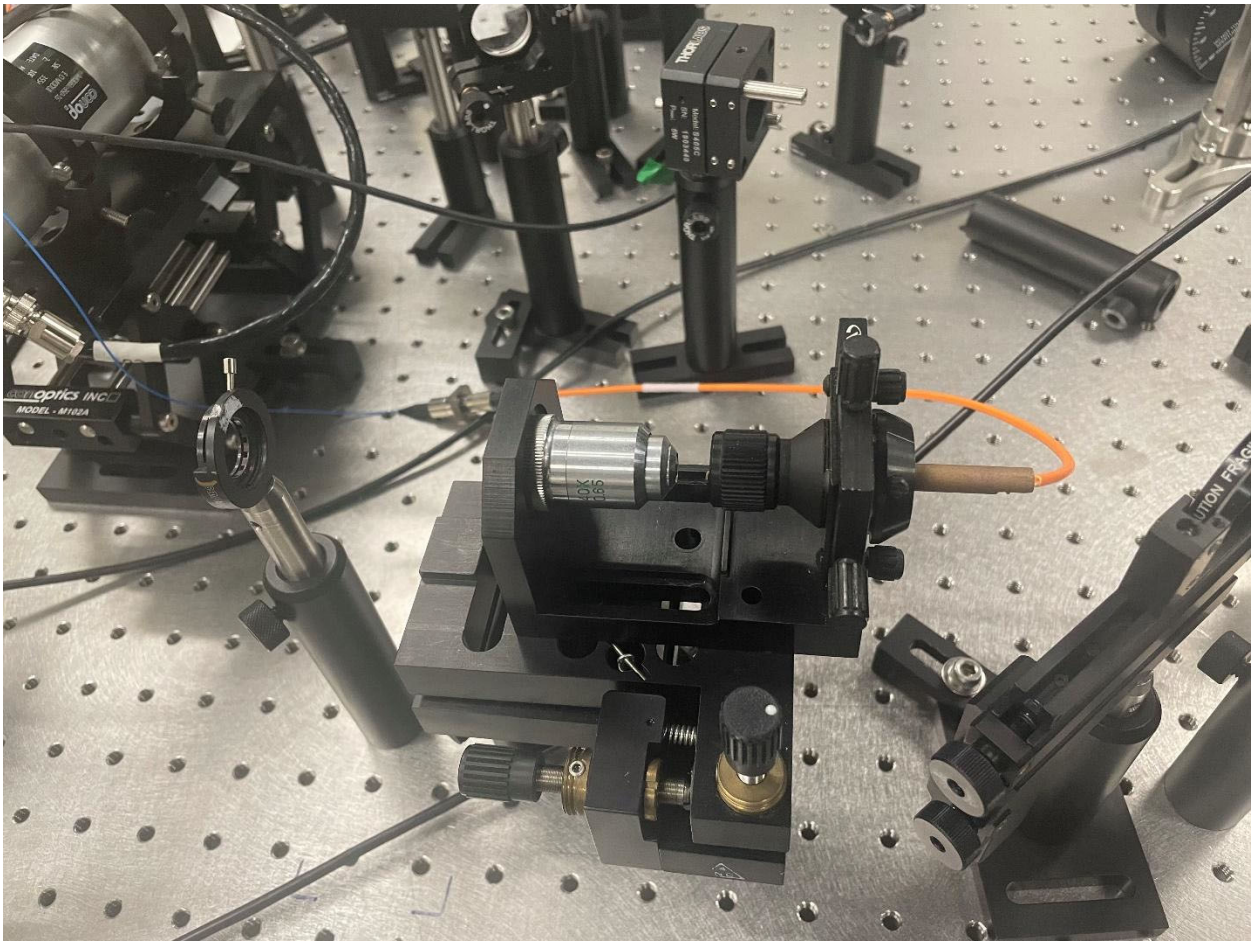

Figure 5.1.4: This apparatus is used to pair the free space laser into the stripped multimode fiber. It uses an objective and 2 axis adjustment knobs to focus the light into the fiber core.

With a modulated pump coupled into the fiber, we were able to initiate a modulated heating event on the inside of the transducer. With filters for the blue light, we are able to see just the green light in the photodetector. Initially, we used a chopper and were able to see a thermoreflectance signal, as indicated by a drop in signal when either the probe or the pump was turned off. Then we moved from the chopper to the EOM and ran sweeps on each of the fibers that we made in the cosputterer (Au, 5% Ti 95% Au, 10% Ti 90% Au, 10nm Ti 90nm Au).

5.2 Fiber Scan Results

Results for the fiber sweeps are seen in Figure 5.2.1.

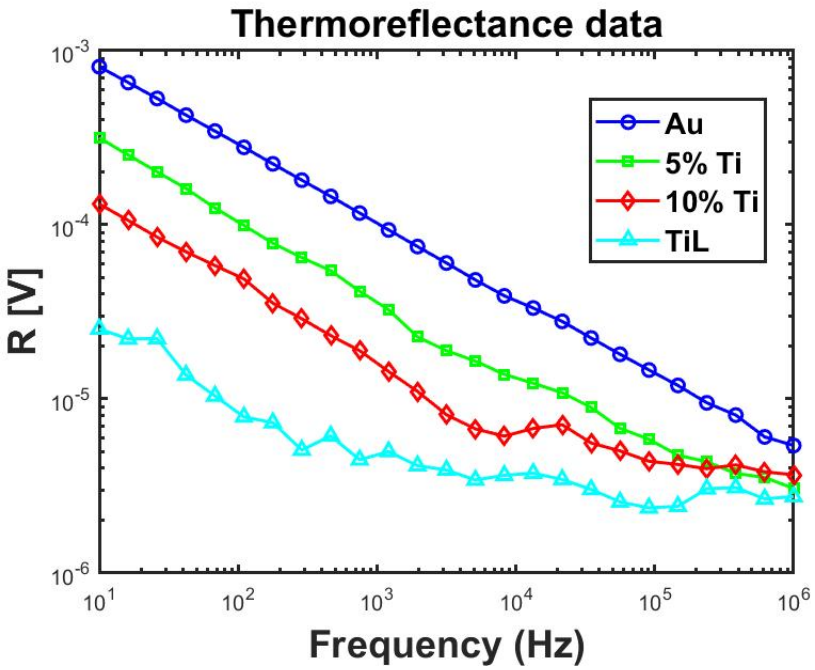

Figure 5.2.1: The thermoreflectance signal for each fiber. Note that the scale is logarithmic. The gold fiber has a considerably higher signal than the other samples. Besides the Ti Layer fiber, the others show a reasonable signal that is a smooth curve with frequency dependence.

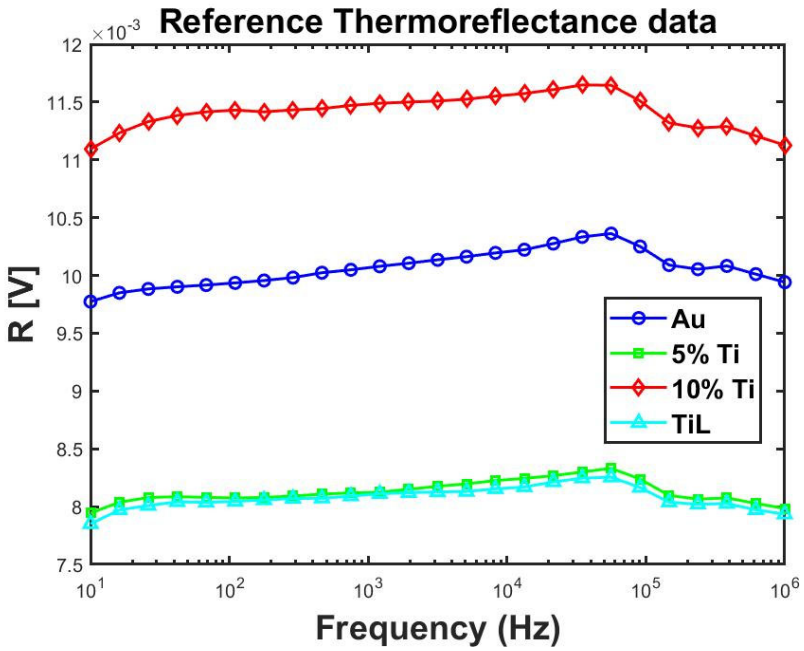

Figure 5.2.2: This is the reference signal magnitude which is the pump laser with no probe and the filters removed for the system. We see that the each sample is returning a strong reflection from the fiber tip.

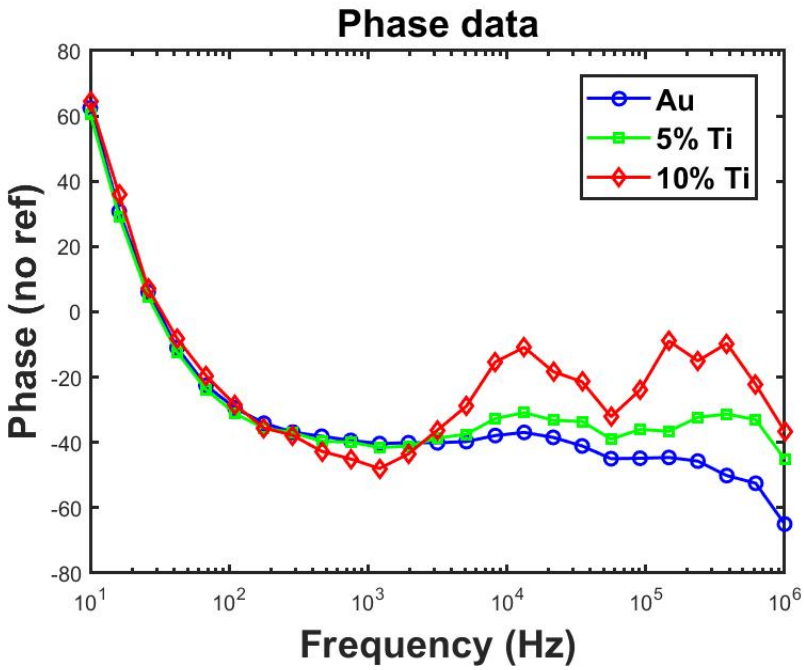

Figure 5.2.3: The graph above shows the raw probe phase. We observe smooth a curve for all three samples up to a kHz before observing patterns that do not fit the existing trend. This may be due to a lower thermoreflectance signal.

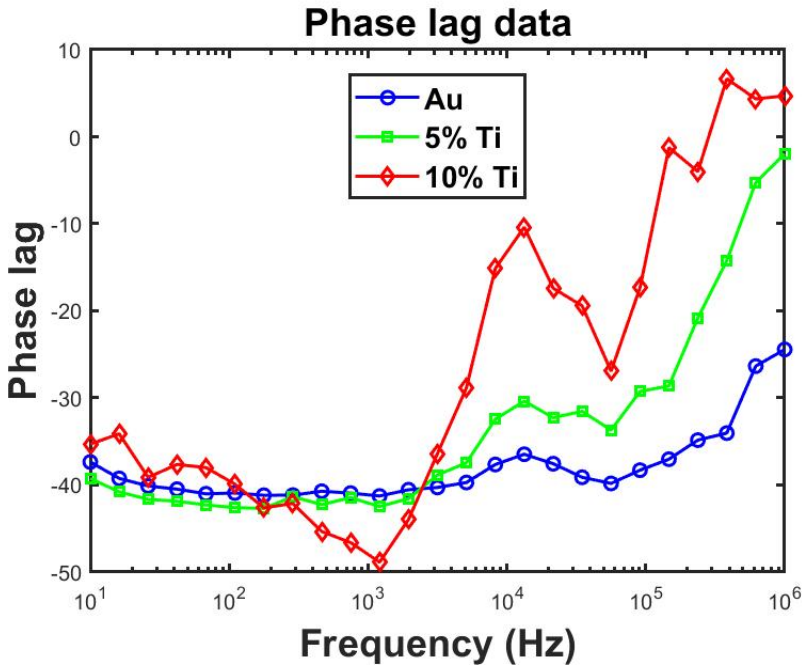

Figure 5.2.4: This is the phase lag from the fiber samples. Phase lag is what we use in our model to fit and so this represents the data that will eventually be used to determine the properties of the surrounding material.

These results show **smooth, frequency dependent** data from a fiber FDTR system. Ideally we would not have an external free space pump paired in, but it is a significant display of the promise of the system and its ability to produce frequency sweeps.

Conclusion

Through many avenues, we have made advances towards an all fiber FDTR system. First, the simulation of our fiber probe in COMSOL permitted a sensitivity analysis to be done for the system. This led to findings for how several parameters such as conductivity of the transducer, thermal boundary conductance with the transducer, could affect sensitivity to the surroundings thermal properties. Along with other experimental methods, the Free Space FDTR system was

set up and used to characterize novel transducer alloys. We found a decreased thermoreflectance with the addition of Ti in the alloys with pure gold at 2.6x10^4 K^{-1} while 5 % was at 2.27x10^4 K^{-1} and 10% at .764x10^4 K^{-1}. We found a similar result with the Ti series, with the thermo reflectance decreasing sharply and then leveling once it is dominated by Ti, going from 2.6x10^4 K^{-1} to 1.12x10^4 K^{-1}. We have constructed a complete prototype of the all-fiber system and have obtained an entirely internal thermoreflectance signal from our novel coated transducers. Using the data from our model study and transducer study, an optimal transducer will be able to be created for future use with the system. While the data from the fiber cannot currently be fit to the data using our COMSOL model, the preliminary data is a significant step in proving the viability of the type of system. Future work should be done to integrate a fiber pump laser and AOM, better understand the coating process of the fibers through more coating regimes and SEM imagery, and integrate a fiber-based filter to eliminate some of the losses in the current free space filter set up. With those improvements we should be able to validate the system with liquids of known thermal conductivity and produce proper fits with our model.

References

[1] J. Choi and J. C. Bischof, "Review of biomaterial thermal property measurements in the cryogenic regime and their use for prediction of equilibrium and non-equilibrium freezing applications in cryobiology," *Cryobiology*, vol. 60, no. 1, 2010, doi: 10.1016/j.cryobiol.2009.11.004.

[2] J. Liu and Z. S. Deng, "Nano-cryosurgery: Advances and challenges," *Journal of Nanoscience and Nanotechnology*, vol. 9, no. 8. 2009. doi: 10.1166/jnn.2009.1264.

[3] A. N. Smith, N. R. Jankowski, and L. M. Boteler, "Measurement of High-Performance Thermal Interfaces Using a Reduced Scale Steady-State Tester and Infrared Microscopy," *Journal of Heat Transfer*, vol. 138, no. 4, 2016, doi: 10.1115/1.4032172.

[4] D. G. Cahill, "Thermal conductivity measurement from 30 to 750 K: The 3ω method," *Review of Scientific Instruments*, vol. 61, no. 2, 1990, doi: 10.1063/1.1141498.

[5] P. Jiang, X. Qian, and R. Yang, "Tutorial: Time-domain thermoreflectance (TDTR) for thermal property characterization of bulk and thin film materials," *Journal of Applied Physics*, vol. 124, no. 16. 2018. doi: 10.1063/1.5046944.

[6] X. Xie, Z. Diao, and D. G. Cahill, "Microscale, bendable thermoreflectance sensor for local measurements of the thermal effusivity of biological fluids and tissues," *Review of Scientific Instruments*, vol. 91, no. 4, 2020, doi: 10.1063/1.5141376.

[7] J. Park and D. G. Cahill, "Plasmonic Sensing of Heat Transport at Solid-Liquid Interfaces," *Journal of Physical Chemistry C*, vol. 120, no. 5, 2016, doi: 10.1021/acs.jpcc.5b11706.

[8] B. F. Donovan *et al.*, "Strained Polymer Thermal Conductivity Enhancement Counteracted by Additional Off-Axis Strain," *Macromolecules*, vol. 53, no. 24, 2020, doi: 10.1021/acs.macromol.0c01243.

[9] Y. Liu and M. Wang, "Fabrication and characteristics of hydroxyapatite reinforced polypropylene as a bone analogue biomaterial," *Journal of Applied Polymer Science*, vol. 106, no. 4, 2007, doi: 10.1002/app.26917.

[10] A. J. Cauvin, C. Peters, and F. Brennan, "Advantages and Limitations of Commonly Used Nonhuman Primate Species in Research and Development of Biopharmaceuticals," in *The Nonhuman Primate in Nonclinical Drug Development and Safety Assessment*, 2015. doi: 10.1016/B978-0-12-417144-2.00019-6.

[11] R. J. Warzoha *et al.*, "A numerical fitting routine for frequency-domain thermoreflectance measurements of nanoscale material systems having arbitrary geometries," *Journal of Applied Physics*, vol. 129, no. 3, 2021, doi: 10.1063/5.0030168.

[12] R. J. Warzoha *et al.*, "Confined Transducer Geometries to Enhance Sensitivity to Thermal Boundary Conductance in Frequency-Domain Thermoreflectance Measurements," 2021. doi: 10.1115/ipack2021-66842.

[13] M. E. Caplan, A. Giri, and P. E. Hopkins, “Analytical model for the effects of wetting on thermal boundary conductance across solid/classical liquid interfaces,” *Journal of Chemical Physics*, vol. 140, no. 15, 2014, doi: 10.1063/1.4870778.

[14] Warzoha, R. J. W. (2022). DEVELOPMENT OF A NUMERICAL MODEL TO ASSESS SENSITIVITY FOR FIBER PROBE FREQUENCY-DOMAIN THERMOREFLECTANCE MEASUREMENTS. Proceedings of the ASME 2022 Summer Heat Transfer Conference.

[15] Braun, Jeffrey L. et al. “A Steady-State Thermoreflectance Method to Measure Thermal Conductivity.” Review of scientific instruments 90.2 (2019): 024905–024905. Web.

[16] Yazawa, Kazuaki et al. “Understanding the Thermoreflectance Coefficient for High Resolution Thermal Imaging of Microelectronic Devices.” Electronics cooling. Web.